UNIVERSIDAD NACIONAL DE COLOMBIA

Detection of pancreatic malignant tumors based on texture characterization during endoscopy ultrasound video sequences

María Jaramillo González

Universidad Nacional de Colombia
Facultad de Medicina, Maestría en Ingeniería Biomédica
Bogotá, Colombia
2022

Detection of pancreatic malignant tumors based on texture characterization during endoscopy ultrasound video sequences

María Jaramillo González

Thesis or degree work presented as a partial requirement to apply for the title of:
Master in Biomedical Engineering

Director:
Ph.D. MD., Eduardo Romero Castro

Research Line:
Applied Computing - Image Processing
Research Group:
Computer Imaging and Medical Applications Laboratory - CIM@LAB

Universidad Nacional de Colombia
Facultad de Medicina, Maestría en Ingeniería Biomédica
Bogotá, Colombia
2022

Dedico esta tesis a mi familia, por ser mi motor e impulso en cada paso que doy. A mis abuelas Tita, Itas y Titi por mostrarme en la mujer que quiero convertirme algún día. A Tito por enseñarme el gran poder que tiene la dedicación. A mi mamá por ser mi compañera de vida y apoyo incondicional. A mi papá por enseñarme el poder de la solidaridad, la compasión y el valor que tienen los actos de amor.

Agradecimientos

Un agradecimiento especial al Profesor Eduardo Romero, por ser el mejor maestro, por cada una de sus enseñanzas y por su apoyo incondicional. Gracias también a Josué Ruano, por acompañarme, guiarme y enseñarme con toda la buena energía y actitud. Gracias al grupo de investigación CIM@LAB, por brindarme el mejor espacio para aprender y mejorar cada día. Gracias al gastroenterólogo Martin Gómez por brindarme su apoyo, tiempo y experiencia. Infinitas gracias a mi familia por ser mi apoyo incondicional, por llenar mi vida de amor y nunca permitir que me sintiera sola. Gracias a mis amigos de la maestría y especialmente a Moni y Tati por ser mi compañía en los momentos más felices y apoyo en los más difíciles. Gracias a Molly por ser mi compañera fiel y refugio siempre. Y por último y más importante gracias a Dios por poner cada una de estas personas en mi camino, por guiarme en este proceso y acompañarme.

Resumen

Detección de tumores pancreáticos malignos basado en la caracterización de textura durante secuencias de video de ultrasonido endoscópico

El Cáncer de Páncreas (CP) fue la séptima causa de muerte por cáncer en el mundo en 2020. Es uno de los más agresivos y en la mayoría de los casos se diagnostica en etapas avanzadas por su respuesta asintomática. El diagnóstico del CP se realiza mediante técnicas de imágen como ultrasonido (US), tomografía computarizada(TAC), resonancia magnética(RMN) y Ecoendoscopia(EE). Aunque la EE tiene la más alta sensibilidad, el proceso de entrenamiento de los especialistas requiere más de 150 procedimientos supervisados, convirtiendose en un procedimiento altamente dependiente de la experticia del gastroenterólogo y del manejo de las múltiples fuentes de ruido durante el procedimiento. Por lo tanto, es deseable un segundo lector para apoyar el procedimiento y asistir el proceso de entrenamiento. Se han desarrollado estrategias computacionales para apoyar la detección del CP, pero son semi-automáticos en la práctica y altamente suceptibles a las fuentes de ruido. La principal contribución de este trabajo es el desarrollo de una estrategia automática para detectar CP en secuencias de video completas de procedimientos de EE. El método describe los eco-patrones en imágenes de EE utilizando el algoritmo "SURF"por sus siglas en inglés. Se definen y describen un conjunto de puntos de interés correlacionados en un análisis multiecala y se filtran las fuentes de ruido que usualmente no se correlacionan entre escalas. Luego, las imágenes con CP se diferencian mediante una clasificación binaria utilizando métodos de soporte vectorial y árboles de decisión. Adicionalmente, el método se evalúa utilizando una base de datos pública construida en este trabajo con 55 casos en total. Finalmente, el rendimiento se compara con los enfoques típicos de aprendizaje profundo, obteniendo un rendimiento de 92.1 % y 90.0 %, respectivamente. Adicionalmente, el metodo propuesto es estable en experimentos al adicionar ruido, en los que las redes fallan en mantener un rendimiento similar.

Palabras clave: Cáncer de páncreas, adenocarcinoma, detección, diferenciación, ecoendoscopia, clasificación de imagenes.

Abstract

Detection of pancreatic malignant tumors based on texture characterization during endoscopy ultrasound video sequences

Pancreatic Cancer (PC) is one of the most aggressive cancers, constituting the seventh leading cause of cancer-related death globally in 2020. Usually, the asymptomatic response of PC causes the delayed diagnosis of the disease. Diagnosis of PC usually includes ultrasonography (US), computed tomography (CT), magnetic resonance (MRI), and endoscopic ultrasound (EUS). Although EUS is the diagnostic method with the highest sensitivity reported, the procedure is highly operator-dependent. A gastroenterologist requires more than 150 supervised procedures to interpret the anatomy blurred by several noise sources. Therefore, a second reader may be desirable to support the procedure and assist the training process in a gastroenterology service. Some computational strategies have been developed to detect PC in EUS images, but those methods are semi-automatic in practice and very susceptible to noise. Hence, the main contribution of this work is an automatic strategy to detect PC in complete video sequences of EUS procedures. The proposed methodology describes the mixture of echo patterns using the Speeded-Up Robust Features (SURF) method. A set of interest points are defined and described correlating the echo patterns in a multiscale analysis, and filtering the noise sources, usually uncorrelated among different scales. Then, images with PC are differentiated by a binary classification method, evaluating Support Vector Machines and Adaboost models. Additionally, the proposed method is assessed using a public EUS database constructed and released in this work, with 55 cases. Finally, the proposed method was compared with typical Deep Learning approaches, reaching an accuracy of 92.1 % and 90.0 %, respectively. In addition, the method herein proposed is also stable in experiments with added noise, while the nets fail to maintain a similar performance.

Keywords: Pancreatic cancer, adenocarcinoma, detection, differentiation, endoscopic ultrasound, Echoendoscopy, image classification

Content

Abbreviations

Abbreviation	Meaning
$ACADI$	Asociaciones Colombianas del Aparato Digestivo
$ARFI$	Acoustic radiation force impulse
AVI	Audio Video Interleave
$B-mode$	Brightness-mode
CA19-9	Carbohydrate antigen 19 to 9
$CH-EUS$	Contrast-Enhanced Echoendoscopy
CP	Chronic Pancreatitis
CSV	Comma-separated values
CT	Computed Tomography
$CPRM$	Colangioresonance
EUS	Echoendoscopy
FNA	Fine-needle aspiration
FP	Focal pancreatitis
HUN	Hospital Universitario Nacional de Colombia
$IPMNs$	Intraductal papillary mucinous neoplasms
$MATLAB$	MATrix LABoratory Software
MRI	Magnetic Resonance
NP	Normal Pancreas
PC	Pancreatic Cancer
PCA	Principal Component Analysis
PET	Positron-emission tomography
$PNENs$	Pancreatic neuroendocrine neoplasms
RoI	Region of Interest
$SIPAIM$	Symposium on Medical Information Processing and Analysis
$SPIE$	International society for optics and photonics
SR	Strain Ratio
$TIFF$	Tagged Image File Format
TNM	Classification of Malignant Tumors
$UGEC$	Unidad de Gastroenterología y Ecoendoscopia
$UICC$	Union for International Cancer Control
US	Ultrasound

Abbreviation	Methods
CNN	Convolutional Neural Networks
$mRMR$	Minimum Redundancy Maximum Relevance
RBF	Radial Basis Function
$SURF$	Speeded-Up Robust Features
SVM	Support Vector Machine

Abbreviation	Metrics
ACC	Accuracy
$AUROC$	Area Under Receiver Operating Characteristic
FP	False Positives
FN	False Negatives
TP	True Positives
TPR	Sensitivity - true positive rate
TN	True Negatives
TNR	Specificity - true negative rate

List of Figures

List of Tables

1. Introduction

1.0.1. Functions of the pancreas

The pancreas is a gland of approximately 10 to 25 cm in length, located on the posterior abdominal wall, that plays a vital role in digestion and metabolism processes[54, 48, 70]. For descriptive purposes, the pancreas is divided into three regions: a head, a body, and a tail[45, 70, 48], as shown in Figure **1-1**. Furthermore, the pancreas is a mixed gland composed of two types of tissues: the exocrine cells that secrete digestive enzymes required in the digestion process and the endocrine cells that produce hormones necessary for the metabolism process[48, 45, 54, 70]. Exocrine tissue is composed of clusters of acinar and pancreatic stellate cells involved in the main disorders of the pancreas, including Pancreatic Cancer (PC) and Chronic Pancreatitis (CP)[54]. Unfortunately, the deep location of the gland and the closeness with vital structures make the pancreas inaccessible to physical examination and convert the surgery into a hazardous task[45].

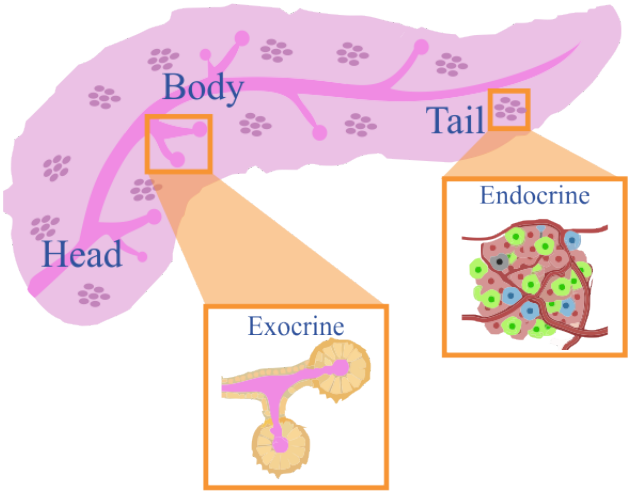

Figure 1-1.: Pancreatic Gland: exocrine component is composed of Acinar Cells and endocrine by Islet Cells.

1.0.2. Natural history of pancreatic cancer

Pancreatic Cancer (PC) is a consequence of a successive accumulation of gene mutations that evolve from pre-malignant lesions to fully invasive cancer[25]. Pancreatic tumors are classified into two main categories: exocrine and endocrine. Approximately 85 to 90 % of the cases are exocrine tumors. Moreover, ductal adenocarcinoma (mutations originated in the ductal epithelium) is almost 90 % of malignant pancreatic tumors. Typically, PC affects patients in their seventh decade of life, most with metastasis or surgically inoperable disease[84].
PC was the seventh leading cause of cancer-related death globally in 2020 and the ninth in Colombia in 2017[74, 7]. In 75 % of the cases, PC is diagnosed at advanced stages, with one of the lower survival prognoses. The 5-year survival rate ranges between 4 to 7 % and rises to 25 % when the tumor is surgically removable, but the disease is operable only in 9 % of the cases.[73, 40, 81, 51, 78, 31]. Some risk factors of PC are etiological, such as cigarette and alcohol consumption and excess weight[7]. Usually, PC presents as an asymptomatic disease until the mass affects the liver function, obstructs the pancreatic and common hepatic ducts, or causes metastasis[13, 44]. Generally, the symptoms are related to the surrounding structures, organs, nerves, and vessels or systemic effects caused by the chemicals secreted by the tumor. Therefore, the symptoms are variable and nonspecific, like abdominal and back pain, fatigue, weight loss, nausea, and jaundice[84, 13, 44, 51, 31, 78]. Hence, effective early PC diagnosis remains a challenging task.
Even with the recent improvement in the knowledge of the disease, PC remains an illness that is difficult to analyze, detect, and treat. The poor prognosis of PC is owing to the delayed diagnosis, causing inadequate or inefficient treatments when the patient presents distant metastasis or nodal invasion[31, 78]. Although PC is less common than other cancers, the mortality rate is one of the higher. In 2018, the incidence was 458,918 new cases and 432,242 deaths worldwide, achieving a mortality rate of 98 %[6]. The incidence of PC varies across regions by differences in diagnostic practices[46].

1.0.3. Pancreatic cancer screening process

The Pancreatic Cancer screening process includes two kinds of tests: serologic and imaging techniques. Treatment response of the disease is evaluated with serological tests, measuring different biomarkers like carbohydrate antigen 19 to 9 (CA19-9), carcinoembryonic antigen, alpha-fetoprotein, chromogranin A, neuron-specific enolase, pancreatic polypeptide, and functional neuroendocrine tumor[40, 84]. However, PC diagnosis and staging are performed using imaging techniques, such as Ultrasound, Computed Tomography, Magnetic Resonance, or Echoendoscopy.
The evaluation process of PC is shown in Figure **1-2**. Usually, the first practiced test is the abdominal Ultrasound (US) because of its noninvasive component, low cost, and high availability. However, the entire pancreas is difficult to visualize, making the detection of tumors a challenging task[44, 76]. Therefore, when the suspicion of PC is strong is practiced

other imaging techniques like Computed Tomography (CT), Magnetic Resonance (MRI), Positron Emission Tomography (PET), or Echoendoscopy (EUS). When a pancreatic tumor is detected, a biopsy is acquired to evaluate the malignancy of the lesion. With EUS, the sample is collected immediately by the EUS-guided fine-needle aspiration (EUS-FNA) procedure[44, 50]. However, when the tumor is detected using CT, MRI, and PET is necessary to practice another exam to collect the biopsy. Hence, EUS is the only method to diagnose and stage PC at the same procedure[52, 76]. The general EUS sensitivity is ranged from 87 to 100 %[51, 55, 16], and the procedure is particularly helpful to detect tumors smaller than 30 mm[51]. Therefore, detection of smaller tumors implies the diagnosis of the disease in early stages, even in asymptomatic patients with risk factors of PC, such as a family history of cancer, specific gene mutations, and Peutz−Jeghers syndrome, among others. Some studies implement pancreatic surveillance protocols using EUS and MRI to detect precursor lesions or earlier stages of cancer, detecting a potentially curable disease and improving the prognosis[19, 22].

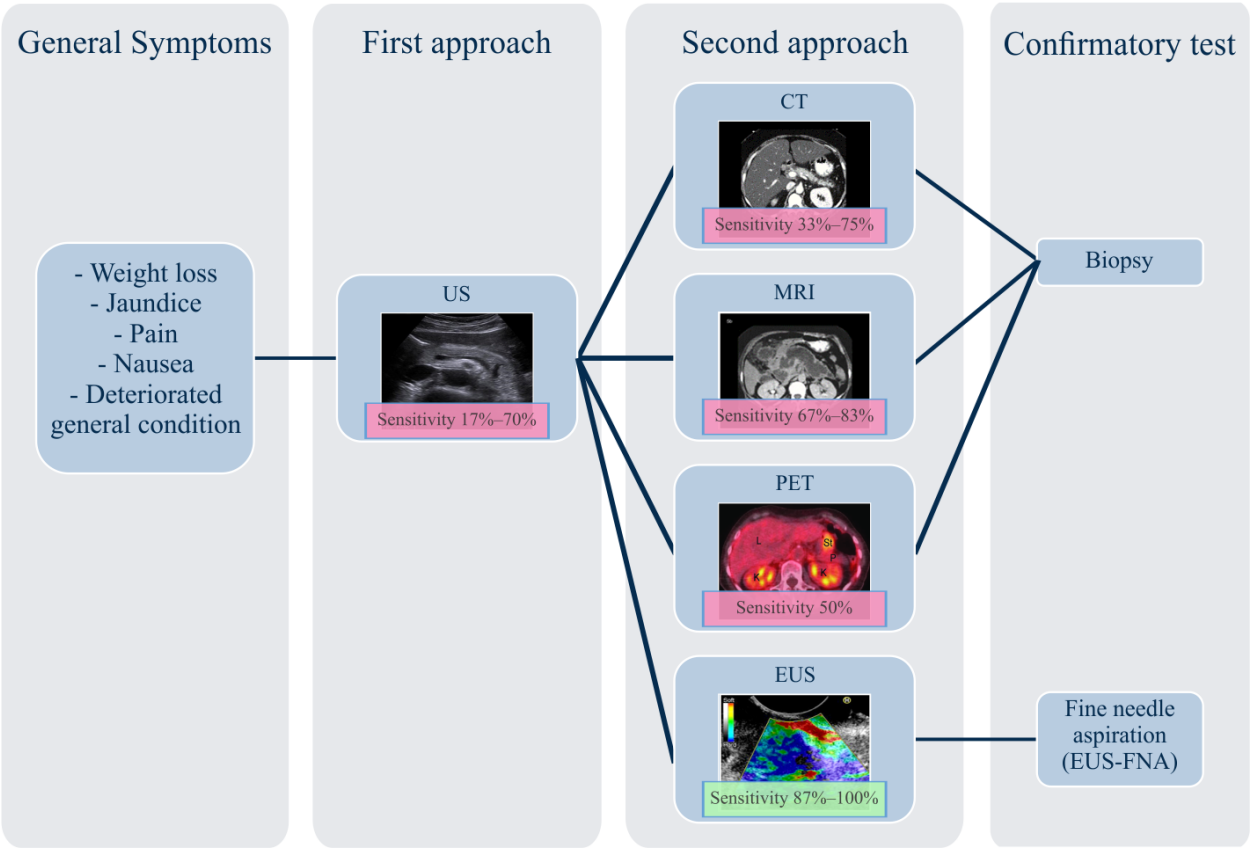

Figure 1-2.: Typical evaluation process of Pancreatic Cancer and the sensitivity of the procedures involved in the detection of PC (Adapted from [50, 51, 31, 40, 16]).

With the clinical exam and the results of imaging techniques, the doctor defines the TNM score, considering three components: the primary tumor size, the presence of metastasis in

the lymph nodes, and the presence of distant metastasis, as shown in Figure **1-3**. The TNM classification for pancreatic tumors in the UICC TNM Atlas[24] is shown in Table **1-1**.

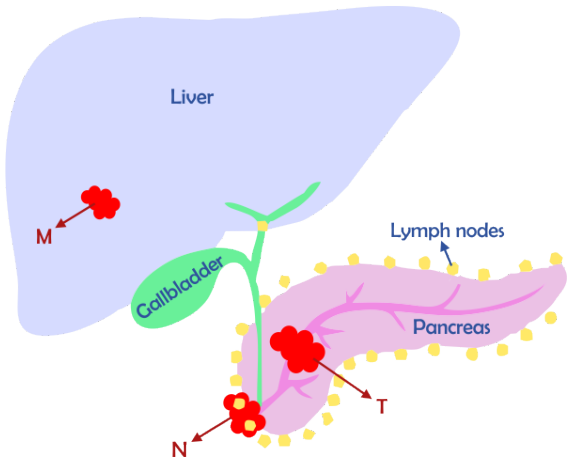

Figure 1-3.: TNM staging system of pancreatic cancer.

T: the extent of the primary tumor	
TX	Primary tumor cannot be assessed
T0	No evidence of primary tumor
T1	Primary tumor limited to the pancreas, 2 cm or less in the largest dimension
Tis	Carcinoma in situ
T2	Tumor limited to the pancreas, more than 2 cm in the largest dimension
T3	Tumor extends directly into any of the following: duodenum, bile duct, peripancreatic tissues
T4	Tumor extends directly into any of the following: stomach, spleen, colon, and adjacent large vessels

N: Extent of regional lymph node metastasis	
NX	Regional lymph nodes cannot be assessed
N0	No regional lymph node metastasis
N1	Regional lymph node metastasis
N1a	Metastasis in a single regional lymph node
N1b	Metastasis in multiple regional lymph nodes

M: Absence or presence of distant metastasis.	
M0	No distant metastasis
M1	Distant metastasis as liver or peritoneal dissemination

Table 1-1.: TNM Classification of pancreatic tumors, taken from [24].

1.0.4. Echoendoscopy procedure

Echoendoscopy or Endoscopic Ultrasonography (EUS) is similar to upper gastrointestinal Endoscopy, but in this case, the tip of the endoscope has a high-frequency transducer. EUS procedure is performed in two stages: first, the typical Optical Endoscopy is performed by introducing the probe into the mouth, esophagus, stomach, and duodenum. Then, the Ultrasound(US) mode is activated to scan surrounding organs such as the pancreas, kidney, liver, and gallbladder. Therefore, the US technique enables the detection of lesions in the target organs because with this technique could be differentiate soft tissues and water structures, and also, some general ultrasonic signs could be observed, such as the location, size, internal and surrounding echo patterns, and borders of the lesions. Finally, when the tumor is localized, the samples for histological examination are acquired using the EUS-guided fine-needle aspiration(EUS-FNA) procedure.

US image is composed of reflected ultrasound waves affected by the acoustic impedance of the tissues. Image construction depends on the transducer configurations to screen the waves in a specific time and space. US waves could be interpreted using amplitude (A-mode), brightness (B-mode or C-mode), motion (M-mode), or frequency (Doppler). The B-mode is the most common technique used in clinical practice. A linear array is constructed by plotting the intensity of the resulting echoes as a two-dimensional image, using a gray-scale representation to illustrate the amplitude of the returning or reflecting radio frequency waves. B-mode images are composed of defined areas with similar intensities or echo patterns like anechoic, hypoechoic, and hyperechoic, as illustrated in Figure **1-4**. Echo patterns are defined by Echogenicity, which is the ability to reflect or transmit the US waves depending on the tissue composition[30, 56]. Black intensities or anechoic patterns represent tissues that do not return echoes, and white intensities or hyperechoic patterns represent those that highly reflect echoes[57, 71]. Typically, healthy tissues are composed of well-defined areas. For example, the fascia, connective tissues, distal nerves, ligaments, and tendons generate hyperechoic patterns, cartilage and muscles cause hypoechoic patterns, and bones, vessels, veins, arteries, and fat yield anechoic patterns[56]. The normal pancreas appearance is characterized by a homogeneous texture with a finely reticular pattern. Furthermore, the main pancreatic duct has a smooth wall, and the ventral pancreas is relatively hypoechoic compared with the dorsal pancreas[72, 20]. However, tumoral lesions are characterized by a complex and heterogeneous mixture of hyperechoic, anechoic and hypoechoic patterns as a result of necrotic or fluid-filled cystic areas of the lesions[56].

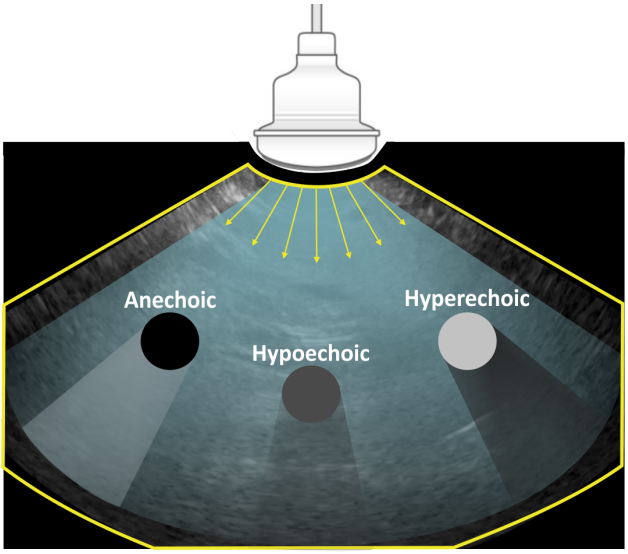

Figure 1-4.: Echo patterns in B-mode US images: hyperechoic, hypoechoic and anechoic.

Image enhancement of Echoendoscopy images

Although the usefulness of the EUS to detect and differentiate pancreatic cancer, EUS is a highly operator-dependent procedure. The EUS utility is influenced by the abilities and skills of the gastroenterologist and by the hard interpretation of the pancreatic anatomy blurred by multiple noise sources. Also, solid lesions of digestive disease are typically hypoechoic, which limits the differentiation between benign and malignant lesions. Therefore, complementary tools such as Elastography and Contrast-Enhanced EUS have been developed to support the diagnosis of the disease, improve the quality of the images, support the staging process and assist the biopsy acquisition[36, 71, 37].

- **Strain Elastography:** superimposed colored map over the B-mode image, acquired without additional devices. Elastography is the most common post-processing technique used in EUS, which evaluates the stiffness of the tissues, measuring their response and deformation when a mechanical compression force is applied and quantifying the displacement of the tissues by a color map. A tumor is defined as malignant or benign using the resultant color patterns, knowing that malignant tumors are composed of necrotic tissues, being more rigid and denser and causing less motion than normal surrounding tissues.[71, 37, 11].

  The first study that reported the use of Elastography for the evaluation of pancreatic tissues was in 2006[17, 37]. Recently, many researchers have been applying the technique to differentiate tissues between pancreatic cancer, benign pancreatic tumors, pancreatitis, and normal pancreas. Initially, the patterns and predominant color of the image were used to classify the lesion between malign or benign[17, 32, 18, 27]. Then quantitative features are calculated to improve the interpretability and objectivity of

the Elastography technique, such as Histogram or Strain Ratio (SR), defining cut-off values or using the features as an input to train Convolutional Neural Networks (CNN)[64, 62, 65]. An example of an Elastography image and the estimation of SR are shown in Figure **1-5**. Moreover, some works that apply Elastography to differentiate lesions between pancreatic cancer and pancreatitis are shown in Table **1-2**.

Autor	**Strategy**	**Patients**	**Metrics**
Giovannini et al., 2009 [18]	Differentiate between malignant and benign pancreatic lesions using qualitative definition depending on the predominant color (blue or green)	Total: 121 PC: 72 PNETs: 16 Benign: 2 CP: 28 Metastasis: 3	TPR: 92.3 % TNR:80.0 % ACC: 89.2 %
Săftoiu et al., 2008[64]	Differentiation between normal pancreas, chronic pancreatitis, pancreatic cancer, and neuroendocrine tumors, using a cut-off value of the hue histogram of a 10-second video	Total: 114 NP: 68 CP: 11 PC: PC PNETs: 3	TPR: 91.4 % TNR:87.9 % ACC:89.7 %
	Multilayer perceptron neural network trained to differentiate between benign or malignant lesions		AUROC: 95.7 %
Iglesias-García et al., 2010[29]	Diagnosis of Malignancy in Solid Pancreatic masses using a cut-off value of the Strain Ratio measure	Total: 86 Malignant: 58 Benign: 28	TPR: 100.0 %; TNR: 92.9 % ACC: 97.7 %
Săftoiu et al., 2012 [65]	Differentiation between pancreatic cancer and chronic pancreatitis, training a Neural Network with the hue histogram of 125 static frames	Total: 258 CP: 47 PC: 211	TPR: 87.6 % TNR: 82.9 % ACC: 84.3 %

Table 1-2.: State of the art of Elastography in Pancreatic Cancer. For these works are computed the following performance metrics: True positive rate or sensitivity (TPR), True negative rate or specificity (TNR), accuracy (ACC), and receiver operating curve (ROC).

Nevertheless, Elastography is a subjective procedure, highly dependent on the specialist expertise[86] and biased by the compression force or maneuver. Moreover, a lesion could have a completely different appearance at different video capturing times[12, 41, 49]. Some studies evaluate the non-usefulness of Elastography in the pancreas because the small shape of the gland causes incomplete images when lesions are larger than 35 mm. Therefore, some tumoral borders are lost, and the strain ratio calculation is hindered

by the difficulty of capturing surrounding reference tissues[35, 26].

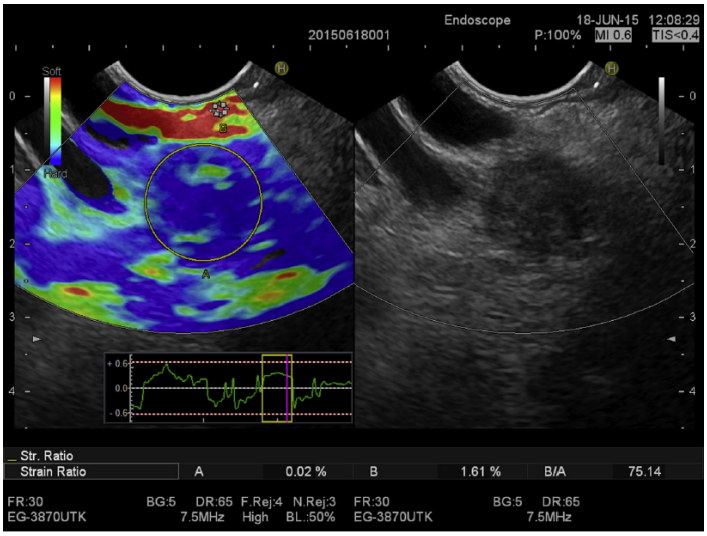

Figure 1-5.: Example of an Elastography image and computation of Strain Ratio as the quotient of a reference area surrounding the mass (B) and a selected representative area from the tumor (A)[29], taken from [28]

- **Contrast-Enhanced Echoendoscopy (CH-EUS):** procedure to evaluate the vascularity of the lesion. This technique supports the delineation of the lesions and improves the diagnostic accuracy to differentiate between benign and malignant solid and cystic pancreatic lesions[63, 37]. The first reported application of CH-EUS was in 1995, using an intra-arterial CO_2 infusion. Then, different echo-enhancing agents were developed to resonate with the stimulus of the US waves, producing low artifact images[37, 36].

  When the enhancement level is maximum, the vascular response is evaluated. Three vascular patterns are defined to represent the differences between the lesion and the surrounding tissues, such as: hypovascular, isovascular, and hypervascular tumor[67]. An example of the lesion enhancement is shown in Figure **1-6**. The hypoenhanced pattern associated with adenocarcinoma achieves high sensitivity and specificity (higher than 90 %), even in small lesions[63, 37]. However, CH-EUS is affected by artifacts such as blooming, overpainting, and motion noises[36].

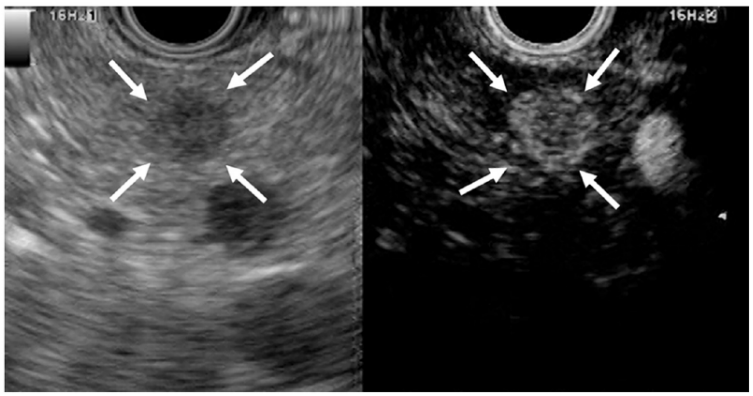

Figure 1-6.: Hypoenhacement of the pancreatic cancer tumor. In the B-mode image (left), the lesion is low echoic (arrows), but in the CH-EUS image (right), the lesion is hypoenhanced in comparison with the surrounding tissues. The figure is taken from [36].

Challenges of Echoendoscopy procedure

Detection of pancreatic masses or tumors during an entire EUS video sequence is a very challenging task because of the several capturing noise sources, namely: a) operator-dependent component, b) tumoral features and c) image noises. The low diagnostic yield is the most significant challenge in EUS tissue acquisition, with the potential to negatively impact patient outcomes yielding improper patient care. A review reported a false negative diagnoses rate of 4 % to 45 % in solid pancreatic masses using EUS-FNA[81]. EUS challenges are shown in Figure **1-7** and explained below.

- **Operator-dependent procedure**
  EUS is a highly operator-dependent technique. In particular, an experienced gastroenterologist requires advanced technical and cognitive skills, i.e., the specific training process takes between 150 and 225 supervised procedures before a specialist achieves the competency and learns a proper anatomic interpretation of a reduced field of vision biased by the ultrasound distortion[55, 85, 59, 8, 30, 79, 5, 81, 80, 86].

- **Tumoral features**
  Typically, a mass is recognized by a rounded shape[83], but malignant masses are characterized by irregular or ill-defined borders[56, 5]. Moreover, the complex anatomy and tissue architecture visualized in US images is difficult to understand[14, 86]. Furthermore, Chronic Pancreatitis (CP) interferes with PC detection, especially at the early stages of PC. The differentiation between the inflammation caused by CP from a discrete neoplasm in EUS images is difficult because the symptoms and imaging findings between the diseases are very similar[2, 68, 55].

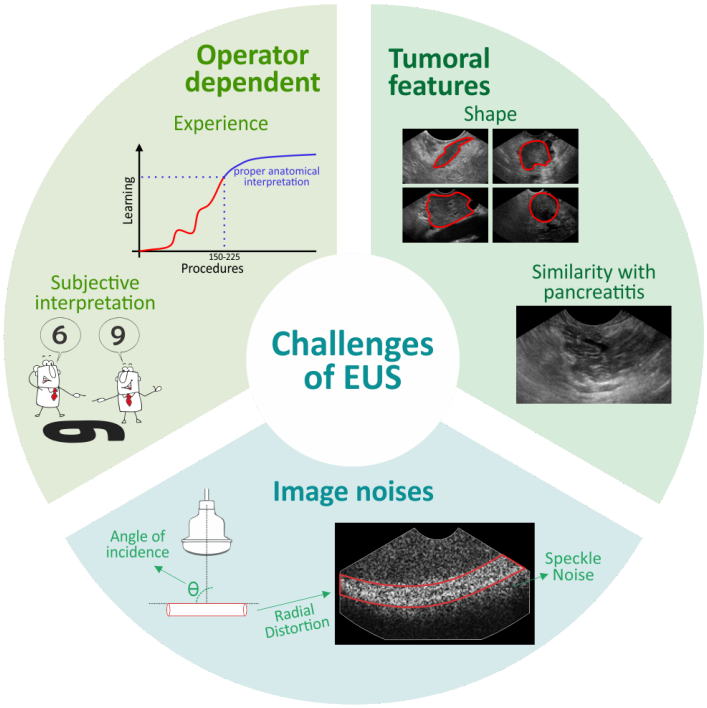

Figure 1-7.: Challenges of Echoendoscopy procedure.

- **Image Noises**
  US images are interfered with many sources of noise that difficult the detection of injuries, such as: the Speckle noise, the curved distortion of the image, and the optimal angle of incidence, which are explained below.

  a Ultrasound images are degraded by the Speckle Noise, an intrinsic artifact produced by the coherent summation of constructive and destructive ultrasound echoes. This artifact is a multiplicative noise that introduces a high-frequency component in the image, changing the intensity level of some pixels. Speckle noise adds a granular pattern in the image caused by electromagnetic interference when the waves reflect on the rough surface and impact between them. This very harmful noise limits the detection of injuries, especially in low-contrast images[47].

  b Curved transducers used in EUS procedures distribute the image intensities radially. The transducers generate a wedge-shaped US beam that affects the appearance of straight anatomical tissues, showing the structures curved, thus, difficulting to understand the ultrasound anatomy[30, 85].

  c The quality of the image is related to the resultant angle between the US waves and the surface of the tissue (angle of incidence). Better images are acquired if the angle is perpendicular or close because more US waves reflect in the transducer. The operator has to achieve the ability to tilt or rotate the probe to obtain adequate images[30].

1.0.5. State of the art of pancreatic cancer detection using Echoendoscopy images

Despite the difficulties of the EUS procedure, the impact of PC on the tissue architecture implies changes that could be extracted using digital imaging processing[14, 86]. Therefore, some computational strategies have been developed to differentiate PC from pancreatitis or healthy tissues in pre-selected EUS images[14, 87, 86, 66]. Besides the application of Elastography images in EUS video sequences as part of Machine Learning workflows, as shown in section 1.0.4-Elastography, other computational strategies use the B-mode images. One approach is textural feature extraction, including measures such as gray level distribution, run-length, co-occurrence matrix, Fourier power spectrum, and energy[86, 14, 53, 87]. Furthermore, classic deep learning strategies have been applied using typical architectures[43, 38], such as ResNet50 or other small-scale-deep architectures adapted for EUS images. Studies that implement the mentioned strategies are presented in Table **1-3**, and the most relevant articles are described below.

- **Machine learning-based frameworks:** Textural analysis has been performed to train and test SVM workflows. For example, Zhang et al.[86] differentiate PC and non-PC patches extracted from EUS images, using a collection of 216 cases diagnosed by two gastroenterologists, of which 153 were confirmed with PC by histopathology analysis. The remaining 63 cases included patients with normal pancreas and chronic pancreatitis. A single frame was selected per case and the tumoral region was delineated by a specialist to extract tumoral RoIs, while the remaining area of the frame was defined as non-tumoral RoI. After the region was pre-selected, a histogram of the pixel intensities was computed from each RoI to extract a set of fractal features of the M-band wavelet transform. Such representation was used to feed an SVM classifier, obtaining 97.98 % of accuracy under a validation scheme of 50 random partitions between the training and testing sets. Similarly, Zhu et al.[87] developed a strategy using frames and RoIs selected by an expert, but in this case, PC samples were differentiated from CP using 262 and 126 EUS images for each class, respectively. A total of 105 statistics were computed for each RoI from the gray level histogram and the wavelet transformation, ending up with 25 statistics selected by the Sequential Forward Selection algorithm. An SVM classifier was trained over 200 trials of randomized experiments, obtaining an accuracy of 94.20 % and specificity of 96.25 %. Although these methods achieve good results, the influence of expert assistance was not determined. Likewise, as previously mentioned, positive and negative regions come from the same frame, making the noise similar, a remarkable reduction of variance since ultrasound is well known for capturing multiplicative noise[47]. This limitation is also an intrinsic weakness of most deep learning approaches, which have been reported to be quite sensitive to noise[42]. In addition, the wavelet analysis applied by both works is not rotation invariant and probably might not capture the heterogeneous patterns of the

tumor regions at different orientations, as usually occurs in a complete exploration.

- **Deep learning-based frameworks:** Neural Networks architectures have been applied in medical imaging analysis, such as VGGNet, LeeNet, GoogleNet and ResNet[43]. For example, Tonozuka et al.[77] designed a small CNN to predict the location of pancreatic tumors using PC and non-PC cases from manually selected images of 139 EUS videos. The network assembled six blocks for feature extraction, each containing convolution, normalization, and activation layers, and fourth max-pooling layers to downsize the features maps. At the end of the network, a convolutional layer obtained a score map with a probability at each position belonging to one of the two classes. The classification task reported 92.4 % of sensitivity and 84.1 % of specificity. Since the remarkable results, the strategy performance depends on the expert selection of frames. On the other hand, Kuwahara et al.[39] developed a strategy to predict whether Intraductal papillary mucinous neoplasms - IPMN (precursor lesions of PC) are malign or benign. The CNN architecture used was the classical but still competitive ResNet50 as the feature extractor, followed by a Global average classification layer. This network was fed with 508,160 images produced by the data augmentation process from 3,970 EUS images recorded from 50 patients diagnosed with IPMN. Performance was evaluated under a 10-fold-cross-validation scheme, reporting an accuracy, sensitivity and specificity of 94.0 %, 95.7 %, and 92.6 %, respectively. In contrast to previous works, this method took frames from a small temporal interval of the EUS video. However, the authors did not analyze a complete exploration of the pancreas, or a differential diagnosis challenge, i.e., pancreatitis cases.

Besides the presented works, Chen et al., Lee et al., and Han et al. [9, 10, 82, 21] analyze ultrasound images of other organs, such as the breast, liver, and esophagus. The general disadvantage of the state of the art methods is the semiautomatic component in real practice and the biased results for the selection of images or patches. Therefore, the lesions are delineated by experienced gastroenterologists when the tumor is clearly defined, and the regions are selected without the tumoral borders. So even with the high reported classification rates, the application scenario is not realistic.

Autor	Strategy	Patients	Metrics(%)	Disadvantages
Norton et al., 2001[53]	A 2-dimensional grid is constructed with the reduced space of fourth extracted features: long-run emphases, gray level nonuniformity, run-length nonuniformity, and run-length percentage. The task is to differentiate between CP and PC	Total: 35 PC: 21 FP: 14	TPR: 100.0 TNR: 50.0 ACC: 80.0	Square RoI to include only the internal structure of the lesion, excluding the edges
Das et al., 2008[14]	Eleven features are selected from 228 statistical parameters of the image using Principal Component Analysis (PCA) to train and validate a neural network to differentiate between NP, CP, and PC	Total: 56 NP: 22 CP: 12 PC: 22	TPR: 93.0 TNR: 92.0 ROC: 93.0	Small patches are selected in most abnormal areas
Zhang et al., 2010 [86]	An SVM classification model is trained using textural features and multifractal vectors of the M-band wavelet transform to diagnose PC	Total: 216 PC: 153 NP: 20 CP: 43	ACC: 98.0 TPR: 94.3 TNR: 99.5	Square patch inside a delineated area with the most enhanced area, avoiding necrotic tissues. Both classes are extracted by the same image
Zhu et al., 2013[87]	An SVM model is trained with the best-selected texture features to differentiate between PC and CP	Total: 388 PC: 262 CP: 126	ACC: 94.3 TPR:96.3 TNR: 93.4	Rectangular RoI inside a manually delineated boundary of the lesion
Kuwahara et al., 2019[39]	A deep learning model is trained to predict malignancy in Intraductal papillary mucinous neoplasms (IPMN)	Total: 50 Benign: 27 Malignant: 23	TPR: 95.7 TNR: 92.6 ACC: 94.0	Selected square patches of EUS images
Tonozuka et al., 2020[77]	A deep learning strategy is trained to differentiate between PC, CP, and NP	Total: 139 PC: 76 CP: 34 NP: 29	TPR: 92.4 TNR: 84.1	10 frames per patient are selected by two experts, which displayed the lesions from the moving images

Table 1-3.: State of the art methods that differentiate Pancreatic Cancer using B-mode image of EUS. For these works are computed the following performance metrics: True positive rate or sensitivity (TPR), True negative rate or specificity (TNR), accuracy (ACC), and receiver operating curve (ROC).

Challenges in post-processing strategies of Echoendoscopy images

Development and evaluation of the methods to support the detection and differentiation of PC in Echoendoscopy procedures have some limitations, such as:

- Diagnostic PC strategies in the state of the art are evaluated in private databases, restricting the development of new methods to improve the classification results or to build clinical applications to support the diagnosis of Pancreatic Cancer.
- The state of the art methodologies are semi-automatic in practice because experts select specific frames or patches, biassing the training and evaluation of the models.
- Speckle Noise is a multiplicative noise that affects classical strategies such as Deep Learning workflows. The impact of this noise does not evaluate in the developed methods.

1.0.6. Contributions

In summary, important advances in detecting PC during EUS procedures have been developed using imaging processing techniques, but those strategies are semi-automatic in practice, very susceptible to noise sources, and only evaluated in private databases, as shown in section 1.0.5. Hence, the strategies do not model a real clinical scenario.
For those reasons, the main contributions of this work are:

- Construction of an annotated Public Database of Echoendoscopy images of the pancreas. The dataset includes cases with pancreatic cancer, pancreatitis, and healthy pancreas (see section 2).
- Development of an automatic method that detects pancreatic cancer frame-by-frame during complete Echoendoscopy videos. The proposed method performs a multi-scale analysis to characterize the echo patterns and filter the noise sources, usually uncorrelated among scales. The method was compared with deep learning-based approaches of the state of the art, achieving competitive results and being less sensitive to typical Ultrasound noises (see section 3).
- Finally, an additional experimentation with the selected Deep Learning approaches was performed, testing different balancing techniques of the dataset and evaluating the impact of pre+post processing methods (see section 4).

2. Pancreatic EUS Database

This chapter is based on the article "Endoscopic ultrasound database of the pancreas" [33], presented at SIPAIM 2020 and published on the SPIE platform. The article summarizes the information from the constructed public database of EUS videos from patients with pancreatic cancer, pancreatitis, and healthy pancreas. ***Abstract:*** *Pancreatic Cancer (PC) is a very aggressive cancer, with a mortality of 98 % and a 5-year survival rate of 6.7 %[40, 81, 51]. Endoscopic ultrasonography (EUS) is the main imaging modality to detect PC in early stages. The reported sensitivity of PC diagnosis for an experienced gastroenterologist ranges from 87 to 100 %[51, 55, 16]. Computational strategies, such as Elastography, have been developed to support mass malignancy diagnosis. However, the studies evaluate their strategies using private datasets, making results incomparable. This work presents an annotated open-access database of Endoscopy Ultrasound videos obtained in the Gastroenterology Unit of the Hospital Universitario Nacional de Colombia and the Unidad de Gastroenterología y Ecoendoscopia. The database consists of a set of 55 cases acquired in the B-mode Ultrasound image, composed of 18 cases with pancreatic cancer, 5 cases with pancreatitis, and 32 cases that include healthy pancreas, liver, and gallbladder. Pancreatic cancer cases were confirmed and staged by pathological examination from biopsy samples and manually annotated per each video frame. Additionally, a preprocessing methodology is presented to highlight the useful echo patterns to differentiate pancreatic diseases.*

2.1. Methodology

Although the advances in pancreatic cancer diagnosis, there are no available public databases of Echoendoscopy videos that include patients with pancreatic cancer to construct new methodologies and compare them with state of the art methods. Hence, an annotated open-access database of Endoscopy Ultrasound videos was constructed. A total of 55 cases were included, divided among 30 women and 25 men whose ages varied between 55 $\pm$ 17 years. The database contains videos of patients diagnosed with pancreatic cancer, pancreatitis, and healthy pancreas. All the videos with tumors are manually annotated and staged with the TNM system by an expert gastroenterologist with more than 20 years of experience. Additionally, a preprocessing step is proposed seeking to highlight relevant texture patterns in EUS images, such as hyperechoic, hypoechoic or anechoic patterns. Therefore, the radial distribution of intensities in EUS images is mapped to a Cartesian representation by applying a polar to Cartesian transformation. Then, a contrast enhancement method was applied to highlight EUS texture patterns. The methodology pipeline is shown in Figure **2-1**.

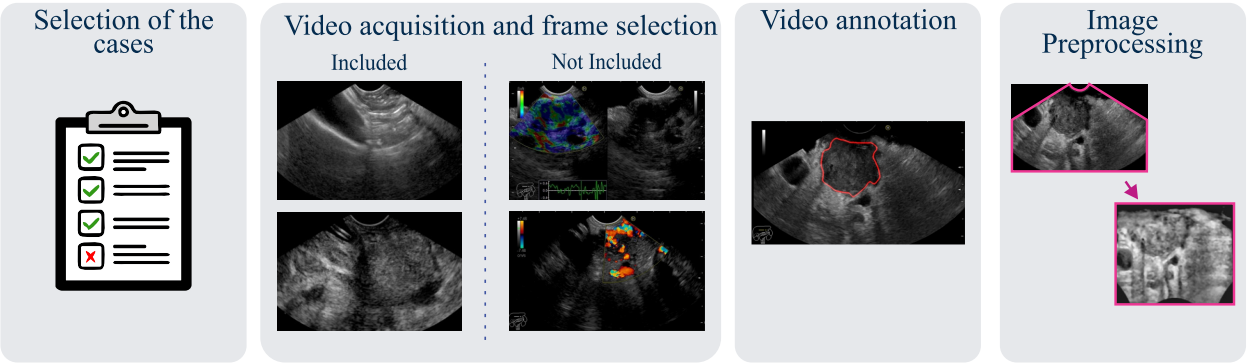

Figure 2-1.: The proposed methodology incorporates four steps: first, a set of cases was captured and selected. Then, the frames with additional procedures were deleted. Afterward, the tumoral cases were delineated. Finally, a preprocessing step was proposed to rearrange visual information to highlight echo patterns.

2.1.1. Selection of cases

A set of cases was captured and selected from the Hospital Universitario Nacional de Colombia (HUN) and the Unidad de Gastroenterología y Ecoendoscopia (UGEC). The database includes patients with pancreatic cancer staged and confirmed by a pathology study as adenocarcinoma, patients with a healthy pancreas, and patients with chronic pancreatitis. All the patients signed an informed consent about the procedure and the permission to use the information exclusively for scientific purposes.

Inclusion Criteria

- Subjects that sign the Inform Consent
- Patients with pancreatic cancer confirmed by biopsy
- Subjects with a healthy pancreas
- Patients with chronic pancreatitis

Exclusion Criteria

- Subjects without clinical history
- Patients with inconclusive pathology in the biopsy

2.1.2. Video acquisition and frame selection

EUS procedures were carried out by an experienced gastroenterologist using an Endoscopic Ultrasound EG-3870UTK (Pentax Medical Company, Tokyo, Japan) combined with a video processor Noblus Ultrasound Scanner (HITACHI, Tokyo, Japan). The EG-3870UTK has a curved and linear-array ultrasound transducer, providing a linear beam. The transducer is configured at a frequency of 7.5 MHz. And the field of view is 120° at a direction of 45° forward oblique. Each procedure was digitized at a conventional gray-scale B-mode linear EUS image, using the video recorder function of the Noblus Ultrasound Scanner. Each video was exported in AVI video format without image degradation or compression. The videos have a spatial resolution of 800 × 500 pixels and a temporal resolution of 15 frames per second. Then, the videos were decomposed into a frame collection, and each frame was cropped to anonymize the image by removing patient, clinical, and device information. Finally, frame spatial resolution was 711 × 457 pixels.
The whole set of images is extracted in TIFF format, but they correspond to exactly the same sequence of the original video. Then, a frame selection process was carried out to select only video intervals with frames without any additional process performed by the specialist such as Doppler, Elastography, or during the Biopsy procedure, as shown in Figure **2-2**.

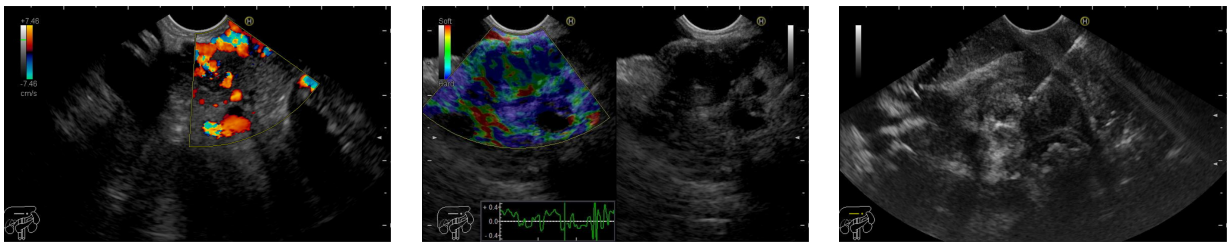

(a) Doppler (b) Elastography (c) Biopsy

Figure 2-2.: Frames with additional procedures not be included.

2.1.3. Video annotation

Recall that the video here corresponds to the set of anonymized TIFF images obtained from the original video sequence. Pancreatic tumors were manually delineated, and the lesions were described using the visual features and the histopathology result. First, an experimented gastroenterologist explores all the frames to select those with the presence of a tumor. Then, the tumoral zone is drawn using a custom interface, obtaining a binary mask of each frame: 1 inside the pathological region and 0 otherwise, as shown in Figure **2-3**

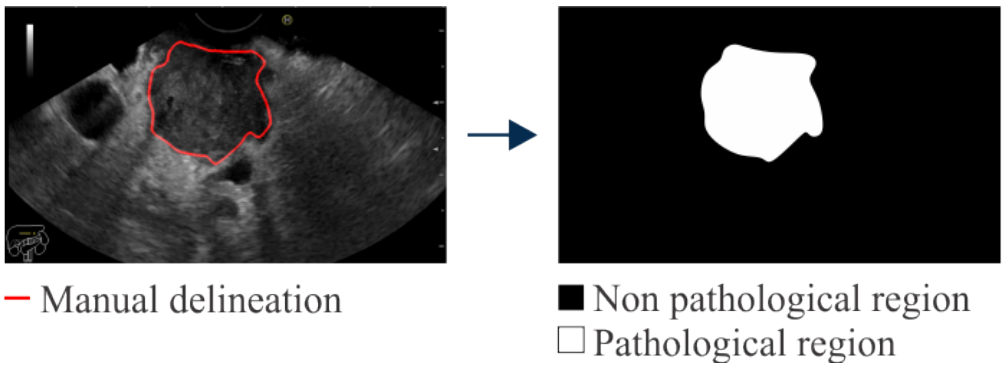

Figure 2-3.: Tumoral zone definition in a binary mask: 1 inside the pathological region and 0 otherwise.

2.1.4. Clinical Information

The patient information is collected in a CSV file, such as the clinical history of subjects, the findings during the EUS procedure, TNM classification, and pathology analysis. First, clinical information such as age, gender, symptoms, another suspicion exam, and treatment is extracted from the medical register. Then, cases with the presence of a tumor are described by the expert specifying the following information: the location of the lesion (head, body, or tail of the pancreas), endoscopic diagnosis, and size of the mass. The size of the tumor is estimated by the expert using the endoscope measurement tool to calculate the distance between two markers positioned at the minor and major axis of the tumor. Furthermore, the TNM score is defined for the tumoral masses based on the clinical findings of the EUS and other imaging exams. Finally, the result of the pathology and stage of the tumor is defined with the EUS-FNA.

2.1.5. Ethical Considerations

This work is carried out following resolution No. 008430 of 1993. Article 11 establishes the scientific, technical, and administrative standards for research in humans. This project is classified as research with minimal risk since the proposed methodology only requires the

use of digital images generated from anonymized endoscopic ultrasound videos, deleting the names or identification IDs of the subjects included in the study.

Construction of the public video collection was approved by the Institutional Review Board of the Research Ethics Committee from the Facultad de Medicina - Universidad Nacional de Colombia (Acta No. 010-083) and conducted according to the Declaration of Helsinki. Written informed consent was obtained from all participants or authorized representatives at each site. Each image was anonymized to protect the identity of the participants. More details about the ethical considerations can be found at https://doi.org/10.1117/12.2581321.

2.1.6. Image Preprocessing

A preprocessing step was proposed to highlight useful echo patterns that describe healthy and tumoral tissues and filter out the Speckle Noise, a multiplicative noise that affects the image introducing a granular pattern that difficult the detection of injuries, especially in low contrast images[47]. Also, the information is mapped to a Cartesian frame to redistribute the intensities distorted by the curved transducers. The preprocessing step is performed in three stages, and the pipeline is shown in Figure **2-4**. First, the center of coordinates of the ultrasound cone is found using the Hough transformation. Then, a conventional polar transformation is carried out to calculate the angle and radius of each pixel. Finally, the speckle noise is corrected by a median filter with a size of 9×9 and a contrast equalization of the histogram is applied using a bell-shaped filter with an alpha of 0.5 as the equalization target. The configuration of filters was qualitatively optimized based on the spatial resolution of video frames and aimed to preserve the echo patterns (textures) and borders of anatomical structures.

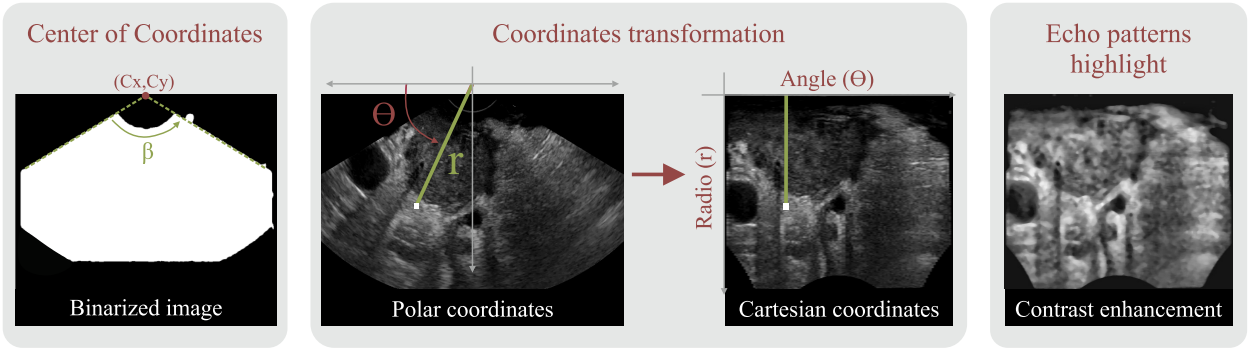

Figure 2-4.: Preprocessing methodology: first, the center of coordinates is found (left), then a polar transformation rearranges the information distributed radially (center), and finally, a contrast enhancement highlights relevant patterns (right).

Polar framework transformation

Curved transducers of the EUS procedure, generate a wedge or cone-shaped image, making straight anatomical structures appear curved. Hence, a polar transformation is applied to redistribute the information, as shown in Figure **2-5**. To apply the transformation, the center of coordinates is found. First, the image is binarized and is found the borderlines of the mask using the Hough transformation. The radial center of coordinates corresponds to the point, external to the image, where the main Hough line crosses with the center of the image. Selection of the best line avoids the problems with images without well-defined borderlines of the cone, as shown in Figure **2-6**. Once this reference is established, a conventional polar to Cartesian transformation is carried out by applying the equations shown in 2-1.

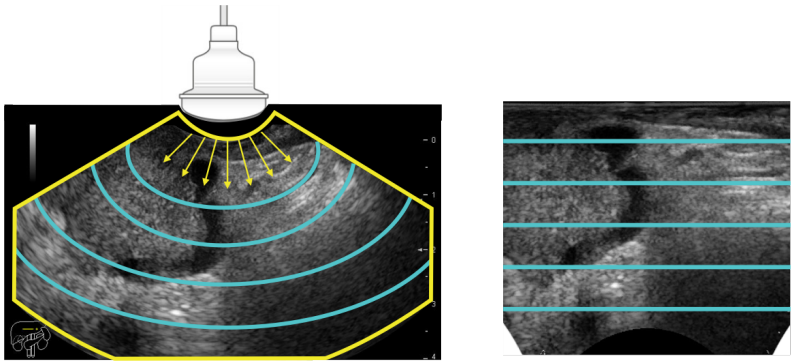

(a) Original image (b) Transformed image

Figure 2-5.: Example of redistribution of information.

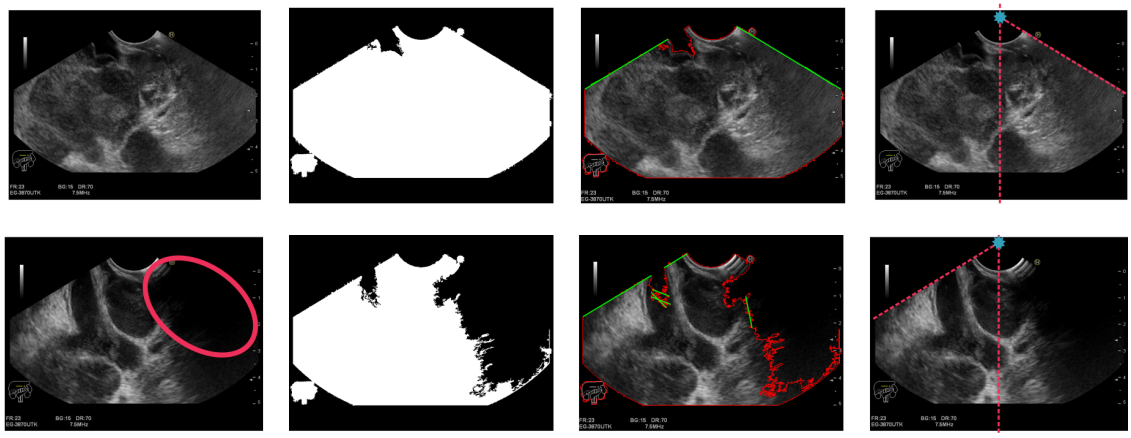

Figure 2-6.: Center of coordinates finding. Each column means: a) original image, b) binarized image, c) edge of the binary mask (red) and candidate lines (green), and d) final line and center of coordinates.

$$\begin{cases} r = \sqrt{(x - C_x)^2 + (y - C_y)^2} \\ \theta = tan^{-1}(\frac{y - C_y}{x - C_x}) \end{cases} \quad (2\text{-}1)$$

Where,
x and y are the Cartesian coordinates of the pixel
C_x and C_y are the coordinates of the center.

Noise reduction and Contrast Enhancement

Medical images are contaminated by different noises that difficult the interpretation task. Ultrasound images are affected by the Speckle Noise, a multiplicative noise caused by the constructive and destructive coherent summation of US waves. This noise significantly reduces the contrast resolution, introducing a granular pattern on the image, known as salt and pepper noise. Speckle noise reduction becomes one of the necessary preprocessing steps in US images. Some filters are applied to reduce this kind of noise. The basic filter is the median, which replaces each pixel with the median value in a neighborhood. As a non-linear filtering technique, the median eliminates the noise but preserves edges and important details of the image[69, 3]. In this work, the size of the applied median filter is 9×9 pixels.

Also, a tumoral zone in Ultrasound images is characterized by a complex mixture of hyperechoic, hypoechoic or anechoic patterns, in contrast with healthy tissues that present well-defined areas of echo patterns[56]. The generated heterogeneous patterns in PC images could be visually imperceptible. Hence, the textures are highlighted by an equalization technique to enhance the image contrasts. The histogram is adapted to a bell-shaped with an alpha of 0.5 as the equalization target.

2.2. Results

The database includes 46 cases from the Hospital Universitario Nacional de Colombia (HUN), acquired between May 2019 to June 2020, and 9 subjects from the Unidad de Gastroenterología y Ecoendoscopia (UGEC), collected between January 2015 to June 2016. The cases were grouped and labeled into three groups: 32 cases as the normal pancreas (NP), 5 cases as chronic pancreatitis (CP), and 18 cases as pancreatic cancer (PC). In total were included 55 patients with 104 videos because some subjects have more than one video. From the videos, 66,249 frames were extracted and labeled as 16,585 with tumor and 49,664 without tumor. The clinical information of all cases is summarized in Figure **2-7** and tables **2-1** to **2-2**. Also, detailed information about each patient is presented in Annexes A and B.

Label	Number of cases	Male	Female	Age (years)
Pancreatic cancer **(PC)**	18	10	8	65.4 ± 10.6
Pancreatitis **(CP)**	5	4	1	45.8 ± 10.1
Normal pancreas **(NP)**	32	11	21	51.4 ± 18.3

Table 2-1.: Summary of cases per type of lesion (label), gender, and age.

Symptoms	Label		
	PC	CP	NP
Abdominal pain	9	3	19
Jaundice	1	0	4
Emesis	2	2	2
Weigthloss	2	0	2
Diarrhea	0	1	2
Other	1	0	6
None	0	0	5
Not reported	9	2	5

Table 2-2.: Summary of cases per symptoms.

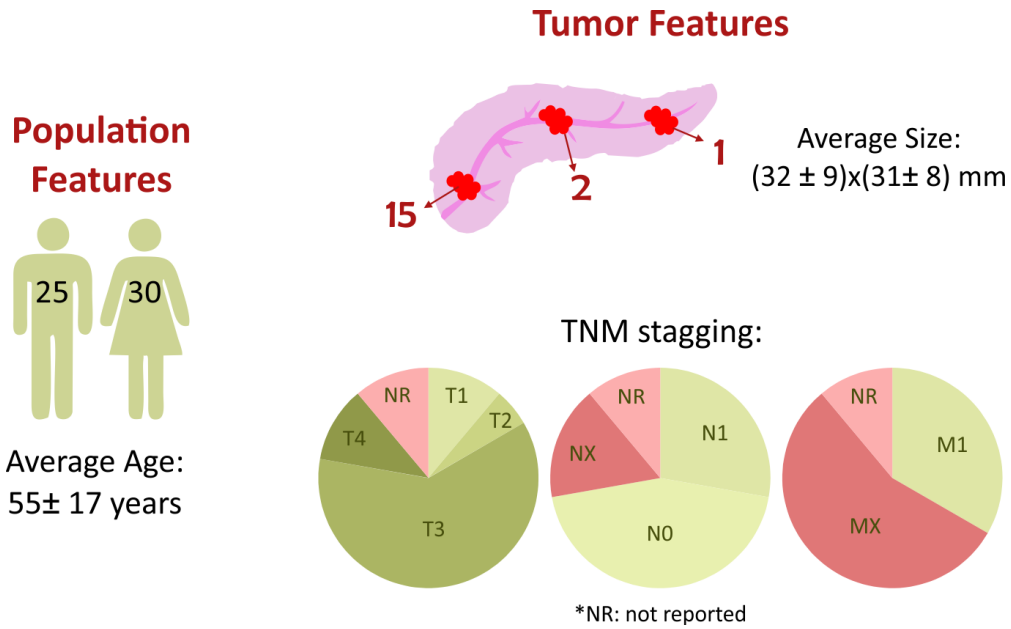

Figure 2-7.: Summary of clinical information of the patients.

The diagnosis of healthy pancreas and pancreatitis cases was confirmed only by endoscopic

ultrasound analysis. The cases with healthy pancreas include patients with other abnormalities, such as: 4 cases with vesicular polyps, 3 cases with gastric lesion, and other diagnoses like ascites, dilated bile duct, cholelithiasis, vesicular microlithiasis, and mucous fold. On the other hand, the cancer cases were diagnosed by endoscopic ultrasound analysis and confirmed by histopathology examination. The location of the tumors was: 15 cases in the head, 2 cases in the body, and 1 case in the tail of the pancreas. The mean size of the tumors is 31 $\pm$ 13.9 mm. The TNM staging score of the cases with pancreatic cancer is shown in Table **2-3**. And each case was manually delineated by an experienced gastroenterologist. Some examples of pancreatic tumor annotation are presented in Figure **2-8**.

Component	**Score**					
	X	**0**	**1**	**2**	**3**	**4**
(T) Primary tumor	0	0	2	1	11	2
(N) Regional lymph node metastasis	3	8	5	-	-	-
(M) Distant metastasis	10	0	6	-	-	-

Table 2-3.: Summary of Tumor staging score (TNM). The score did not report in two cases.

(a) Case C01 (b) Case C02 (c) Case C03

(d) Case C05 (e) Case C07 (f) Case C09

Figure 2-8.: Examples of EUS images with a manual delineation of the tumoral zone (red line) performed by an expert.

The preprocessing methodology was validated qualitatively by a gastroenterologist, comparing the original and preprocessed images, as shown in Figures **2-9** and **2-10**. The echo patterns identification is difficult using the original images because some regions have low contrast(column a). On the other hand, the result of the preprocessing step highlight the

shadowed regions, improving the visualization of the echo patterns and the feasibility of comparing the inside textures with the surrounding patterns(column c).

In summary, the database is organized in folders for healthy pancreas, pancreatitis, and pancreatic cancer cases. Each folder contains a set of images in TIFF format organized as follows: a) the original images of each case without personal information of subjects, b) the preprocessed images, and c) the binary mask as the result of the manual annotation of pancreatic cancer cases. Furthermore, a CSV file contains the clinical information about all the subjects, such as the age, gender, tumor size, location of the tumor, stage of the disease, endoscopic diagnosis, and pathology result. Finally, the database is available on the website http://cimalab.unal.edu.co/?lang=esmod=programid=26 after the user fills out a short online form asking for the complete name, mail, and affiliation.

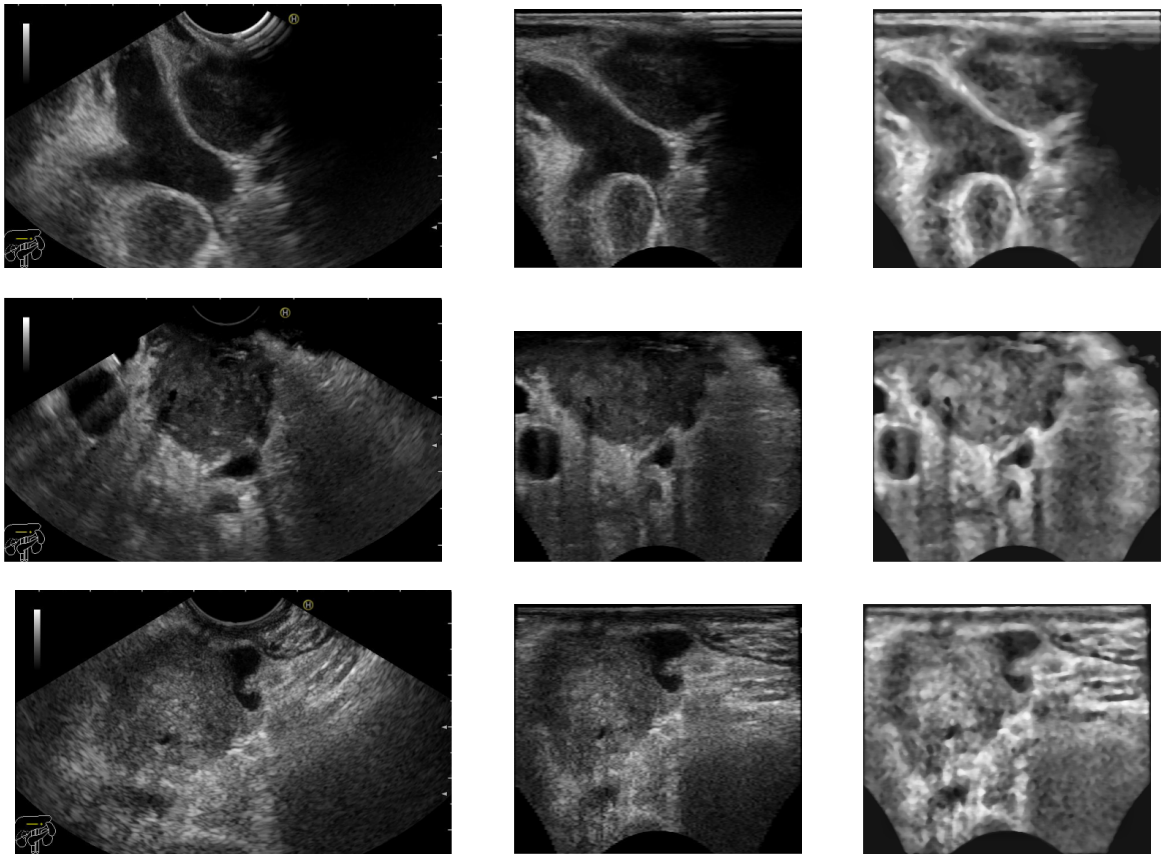

(a) Original image (b) Transformed image (c) Final image

Figure 2-9.: Preprocessing result: each row corresponds to a frame of a particular case, and the columns represent the original images (a), the resulting images after the polar transformation(b), and the final result of the preprocessing step (c).

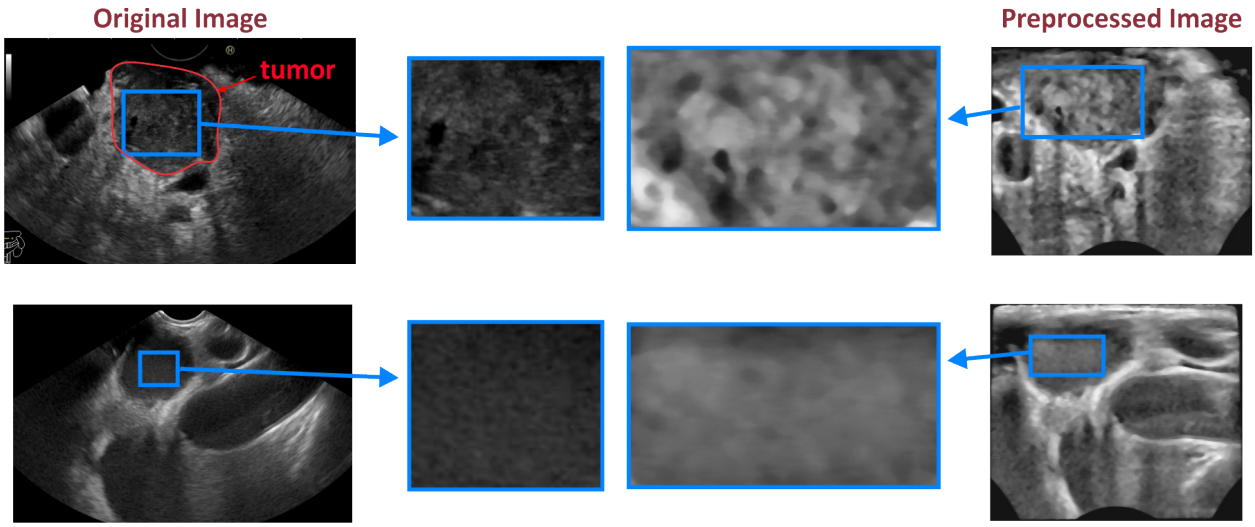

Figure 2-10.: Qualitative result of the preprocessing step. Pattern enhancement of healthy tissues (bottom) and tumoral lesions (top).

2.3. Conclusions

The proposed database builds a publicly available set of videos captured during endoscopic ultrasound procedures of the pancreas. The database contains three groups of cases diagnosed by an expert such as healthy pancreas, pancreatitis, and pancreatic cancer. Therefore, the database may be used to develop diagnostic support tools for the detection and differentiation of pancreatic diseases. Moreover, the database includes tumors smaller than 30 mm, enabling the development of methods to perform an early diagnosis of PC. Furthermore, the database collects patients with pancreatitis, enabling the differentiation between malignant tumors and benign inflammation, a task with higher subjectivity in clinical practice. Finally, the clinical information of the subjects and the tumor description are valuable features to relate the EUS procedure to risk factors and prognosis of the disease.

3. Pancreatic Tumor Detection

This chapter is based on the article "Robust descriptor of the pancreas tissue for automatic detection of pancreatic cancer in endoscopic ultrasonography"[60], published in the Ultrasound in Medicine and Biology journal. ***Abstract:*** *Pancreatic Cancer (PC) has reported mortality of 98 % and a 5-year survival rate of 6.7 %. Experienced gastroenterologists find out 80 % of the early stages with endoscopic ultrasonography (EUS). This paper proposes an automatic second reader strategy to detect PC in an entire EUS procedure, rather than focusing on pre-selected frames as the state of the art methods do. The method unmasks echo tumoral patterns in frames with a high probability of tumor. First, Speeded-Up Robust Features define a set of interest points with correlated heterogeneities among different filtering scales. Afterward, intensity gradients of each interest point are summarized by 64 features at certain locations and scales. A frame feature vector is built by concatenating statistics of each feature of the 15 groups of scales. Then, binary classification is performed by Support Vector Machine and Adaboost models. The evaluation was performed using a dataset with 55 subjects, 18 of PC the class (16,585 frames) and 37 subjects of the non-PC class (49,664 frames), randomly splitting ten times. The proposed method reached an accuracy, sensitivity, and specificity of 92.1 %, 96.3 %, and 87.8 %, respectively. The observed results are also stable in noisy experiments while deep learning approaches fail to maintain similar performance.*

Typically, a tumoral zone is characterized by heterogeneous patterns, in contrast with healthy tissues, usually composed of well-defined areas, i.e., mixtures of hyperechoic, hypoechoic or anechoic patterns[56], as illustrated in Figure **3-1**. This work introduces a novel second reader by constructing a customized descriptor of pancreatic tumors. The method accurately detects frames with a high probability of containing pancreatic adenocarcinoma during endoscopy ultrasound procedures. The proposed descriptor captures the heterogeneous visual patterns of tumoral regions by transforming the image to the SURF space at a particular scale and with a preferred direction. A strong correlation of different intensity gradients at multiple scales in the area surrounding these points captures the altered tissular architecture. Such description demonstrated to successfully differentiate frames with or without pancreatic adenocarcinoma. The presented approach outperformed state of the art deep learning algorithms with lower complexity and training times.

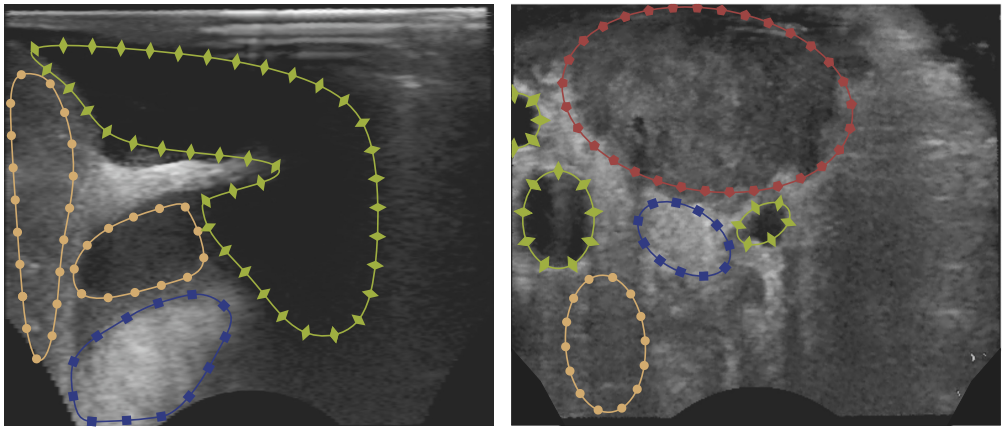

Figure 3-1.: Two frames extracted from EUS videos show the different echo patterns: healthy regions (left panel) are composed of hyperechoic (square), hypoechoic (circle), and anechoic (diamond) patterns, while images with pancreatic cancer (right panel) contain very heterogeneous regions (polygon).

3.1. Methodology

The pipeline of the proposed methodology is shown in Figure **3-2**. First, the radial distribution of intensities is transformed to Cartesian coordinates and then enhanced by histogram equalization. Regions with heterogeneous patterns are located by the Speeded Up Robust Features (SURF) method, which detects points of interest at a specific image coordinate, Gaussian radius (referred to as scales), and orientation[4]. Regions surrounding the detected points, whose size is defined by the Gaussian radius, are characterized by 64 Haar wavelet features describing the regional gradients. The set of obtained regions depends on the number of scales, which is clustered into 15 groups and described by computing different feature statistics per group. A frame is characterized by a relevant set of 256 features found by the

minimum Redundancy-Maximum Relevance (mRMR)[58] algorithm. Finally, two machine learning models, Adaboost and SVM with RBF and Linear kernels, classify images as containing or not malignant tumors. The video acquisition protocol and image preprocessing step are described in chapter 2.

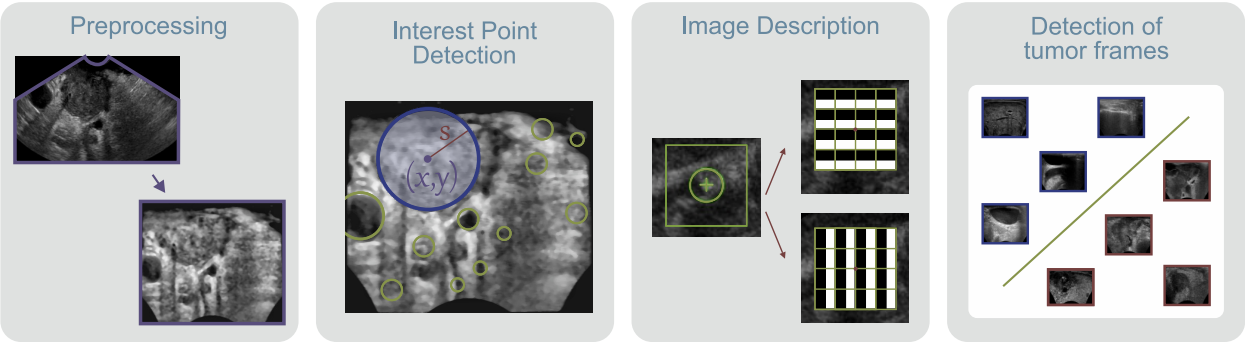

Figure 3-2.: The pipeline of the proposed method incorporates four steps: (a) a preprocessing step rearranges visual information and reduces the speckle noise. Then, a set of interest points are detected (b) and described (c) by the SURF algorithm. Finally, such description was used to train and test machine learning models (d) to classify EUS images between pancreatic cancer and non-pancreatic cancer.

3.1.1. Detecting the Regions of Interest

Echogenicity, the ability to reflect or transmit US waves depending on the tissue composition[30, 56], characterizes tumoral lesions as a complex and heterogeneous mixture of hyperechoic, anechoic and hypoechoic patterns as a result of the tumoral necrotic or fluid-filled cystic areas[56]. A multi-scale analysis by the Speeded-Up Robust Features (SURF) aims to detect points surrounded by regions with heterogeneous patterns[4]. Briefly, a scale-space is generated by a set of Gaussian second-order derivative filters (Hessian matrix) of different Gaussian radii or scales and grouped by octaves and levels. An octave is a set of filters whose size is regularly increased by a pre-fixed step, and the number of levels corresponds simply to the number of filters per octave. The present analysis was carried out with octaves whose increments were 6, 12, and 24, with 5 levels per octave, resulting in Gaussian second-order derivative filters whose radii vary between 1.6 to 16.4 (9×9 to 123×123 window size, respectively). A set of response maps is obtained by convolving each filter with the integral image computed from the US frame. Thus, the scale-space corresponds to the determinant of the per-pixel-Hessian matrix at each response map.

After a scale-space is built, candidate points of interest are those positions with a Hessian determinant greater than 500. A threshold is picked from the minimal level of variation of regions with hyperechoic, anechoic, and hypoechoic patterns. Afterward, a point of interest corresponds to a three-dimensional neighborhood ($3 \times 3 \times 3$) of a candidate point whose center is a Hessian maximum for three consecutive scales and a specific octave. A quadratic interpolation then locates the neighborhood extremum which is approximated by one of the 114 filters with window sizes between 9×9 to 123×123 (Gaussian radius values between 1,6 to 16,4).

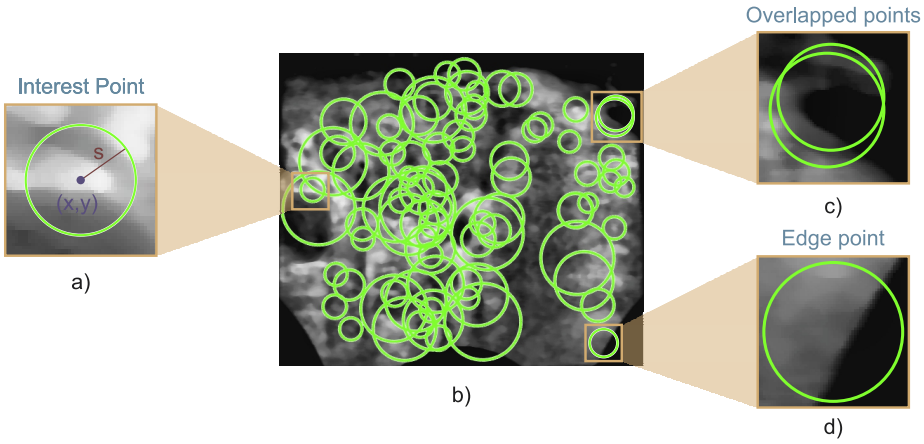

Figure 3-3.: Example of detected interest points over an EUS image(b). Each point is described by a position, scale, and orientation(a). And, overlapped points are deleted (c) or those near the black mask.

Some detected points are deleted following two criteria. First, when the point area overlaps in more than 80 % of the outer cone or remaining black regions after the polar transformation (see Figure **3-3.d**). And when two points are separated by a maximum of 7 pixels on the same scale or two consecutive scales (see Figure **3-3.c**). At the end of the process, each image is represented by a set of interest points described by its position and scale, as shown in Figure **3-3.a**.

3.1.2. Describing the Regions of Interest

Once relevant regions are detected as points of interest, their echographic patterns are characterized by the SURF descriptor as a vector of 64 features. To describe the points, the dominant regional direction is determined by computing the Haar wavelet coefficients in x and y directions within a square whose side length is $4 \times s$ (four times the scale) and which is displaced within a circular area around the point of interest with a radius of $6 \times s$ by applying sample steps of s. The x and y Haar coefficients per sample step are represented with a vector centered at the origin, and a sliding orientation window of size $\pi/3$ adds up these vectors,

obtaining a representative vector for each rotating window. Finally, the direction with the highest magnitude is the dominant gradient orientation. Afterward, a squared area with a size of $20 \times s$ is aligned to this dominant direction, placed around the center of the point of interest, and divided into 16 windows, subdivided into 25 sub-regions. The Haar wavelet coefficients dx and dy in x and y directions are computed for each of the 25 sub-regions. Finally, each of the 16 windows is described by the tetraplet $\left[\sum dx, \sum dy, \sum |dx|, \sum |dy|\right]$, yielding a feature vector with 64 dimensions. This process is shown in Figure **3-4**.

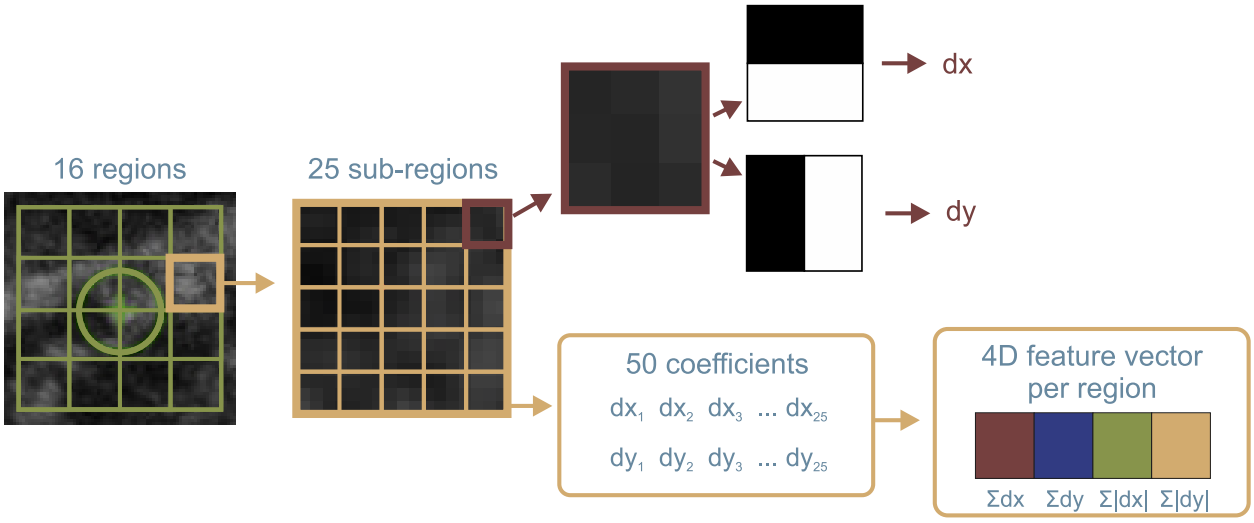

Figure 3-4.: Regions of Interest description workflow. First, an area around the detected point is divided into 16 regions, described by 4 features: $\sum dx$, $\sum dy$, $\sum |dx|$, and $\sum |dy|$ as the result of the Haar wavelet analysis dx, dy within 25 subdivisions of the 16 sub-regions. Finally, the area of the point is characterized by 64 features (16 regions $\times$ 4 features).

At this point, the feature vectors of regions of interest with a similar scale are clustered in 15 groups and a statistic is computed for each feature, i.e., each group is represented as a vector with 64 dimensions, as shown in Figure **3-5**. Different statistics were tested, namely the mean, median, mode, entropy, and minimum and maximum values for the 15 groups. The best representation is set by a feature selection process, as explained below.

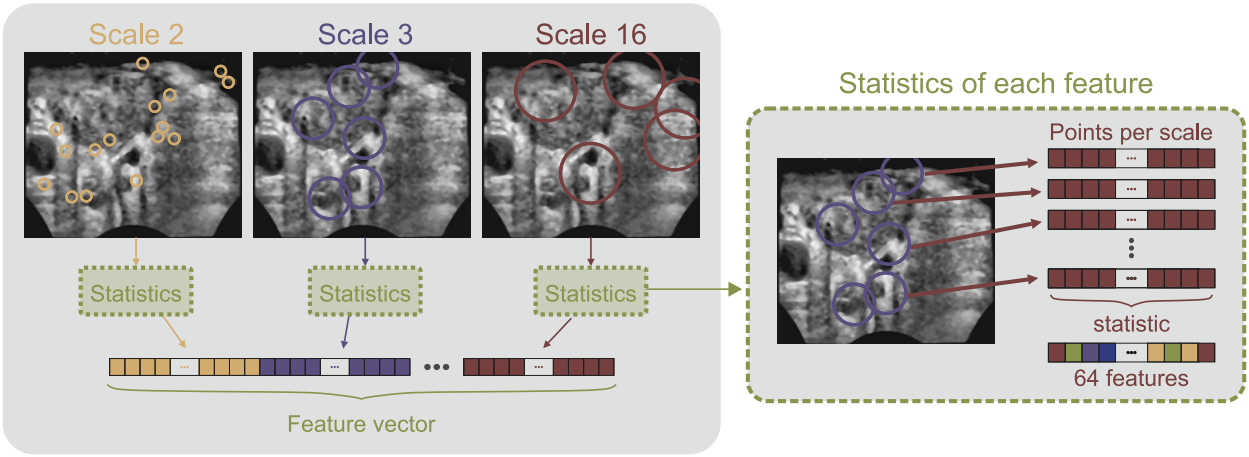

Figure 3-5.: The feature vector that describes an EUS image is computed in 3 steps: First, features of the interest points are grouped by scales. In each group, a statistic is computed for each of the 64 features. Finally, the statistics computed in the 64 features for the 15 groups are concatenated for a subsequent feature selection process.

Selection of most relevant scale and feature statistics:

From the total of 5.760 features, namely mean, median, mode, entropy, and minimum and maximum values from the groups of scales, the minimum Redundancy-Maximum Relevance (mRMR)[58] selected the most discriminant features. A first experiment chose the relevant scales, and then the most important statistics were determined, as shown in Figure **3-6**. Specifically, the first experiment consisted of building, for each group of scales (15 groups), a feature vector concatenating all feature statistics (6 statistics $\times$ 64 features = 384 dimensions), and then the mRMR algorithm selected the twenty most relevant features per group of scales. A counter was storing the number of times a specific statistic was selected as discriminative for the 15 groups. Finally, the statistic with the highest frequency among groups was considered as discriminative, as shown in the top panel of Figure **3-6**. Similarly, in a second experiment, a feature vector concatenates each statistic over all the scales (15 groups of scales $\times$ 64 features = 960 dimensions). Therefore, scales with the highest frequency among groups were considered as discriminative, as shown in the bottom panel of Figure **3-6**. A summary of the resultant cumulative frequency of this process for the ten iterations is shown in Figure **3-7**, being the median the most relevant statistic for the group of scales 2 to 5.

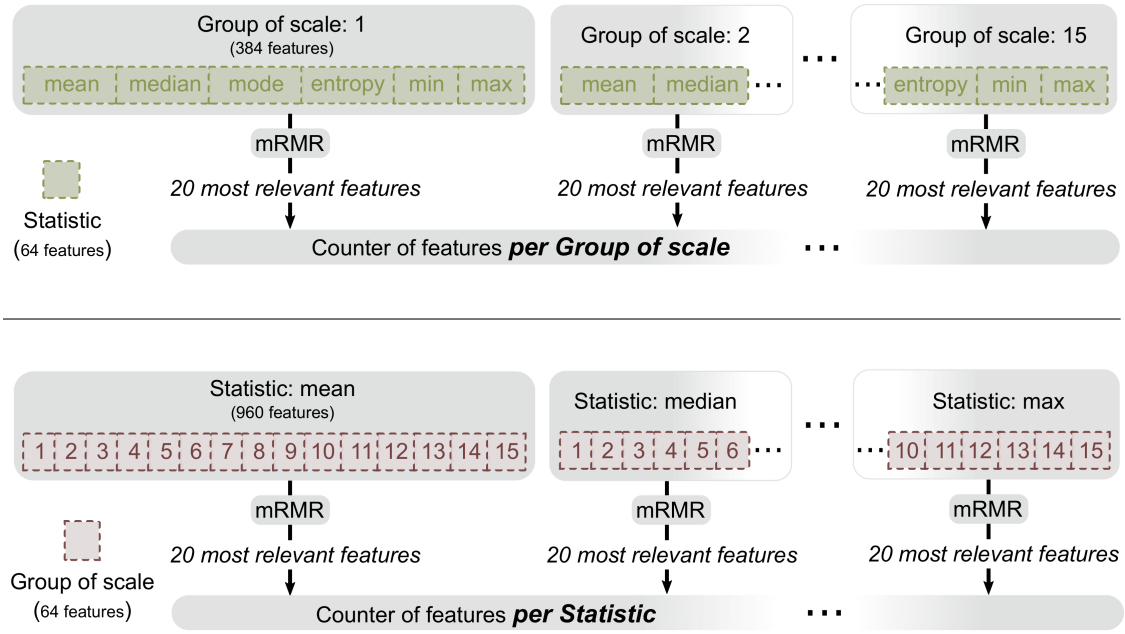

Figure 3-6.: Feature selection process. The top panel shows the process to select the most relevant statistic using the minimum Redundancy-Maximum Relevance algorithm. And in the bottom panel shows the process to select the most relevant groups of scales.

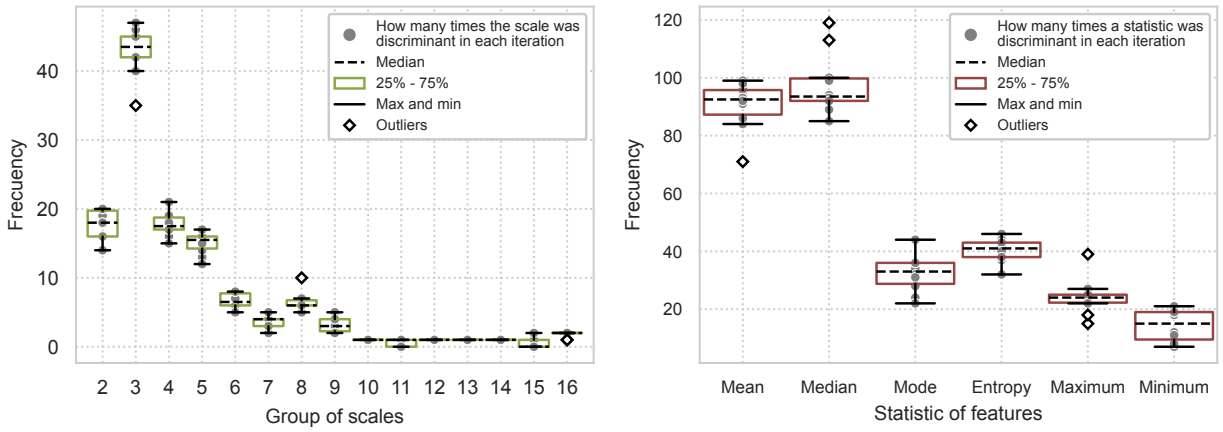

Figure 3-7.: Cumulative frequency for the ten iterations of the feature relevance statistics (right) and scales (left).

From described experiments, the median was chosen after evaluation with the mRMR selector. The resulting feature vector per frame is then built by concatenating the vectors of four groups of scales, from 2 to 5, making a total of 256 characteristics.

3.1.3. Detection of pancreatic tumor frames

A binary classification task consists in selecting frames with a malignant pancreatic tumor (the positive class) against another tissue (the negative class), which stands for images containing other organs commonly observed during an EUS exploration, like the healthy pancreas, the liver, and the gallbladder, or frames with pancreatitis. This classification is performed by a machine learning classifier, trained with a feature matrix extracted from a set of frames used only for training. Each row of the feature matrix corresponds to a feature vector (256 characteristics explained in the previous section) computed from a frame and a label "1" if the class is positive or "0" otherwise. Afterward, the trained model predicts the label from another set of frames for testing, i.e., frames with an unknown label. Two conventional but representative machine learning models are evaluated: Adaboost and SVM with RBF and Linear kernels. Once the model predicts the labels of the video frames, a further refinement consists in filtering out mislabeled frames by a simple strategy that approximates the sequence to a stationary stochastic process within a moving window of 61 frames. This process assigns one to a frame if at least 25 % of the frames within the window are positive.

3.1.4. Dataset

The proposed approach was assessed using EUS videos from 55 subjects of the public database described in chapter 2. The database includes patients in one of the following groups: healthy pancreas, chronic pancreatitis, or pancreatic cancer. Each diagnosed case with pancreatic cancer was confirmed by histopathology examination from biopsy obtained with an EUS-guided fine-needle aspiration (FNA). A high agreement was observed between expert diagnosis and histological confirmation. But the gold standard in this work was the pathology examination, thereby avoiding a second gastroenterologist opinion. Among the cases, 32 patients were reported as having normal pancreas, 18 patients were diagnosed with pancreatic adenocarcinoma, and 5 patients were informed with pancreatitis. Among the normal pancreas cases, three were suspected of having a gastrointestinal stromal tumor, a lipoma tumor compatible with a gastric subepithelial lesion, and an early gastric lesion, respectively. The masses confirmed with PC were manually delineated by a trained gastroenterologist. The lesions were measured on average $32 \pm 9 \times 31 \pm 8mm$. The smallest recorded mass had $15 \times 24mm$, and the largest had $43 \times 38mm$. Most pancreatic tumors (fifteen), were located in the head, while two were reported in the body and one in the tail.

3.1.5. Implementations

All methods were implemented in MATLAB platform v. 2020b (MathWorks Inc., Natick, Massachusetts, USA). The parametrization of each methodological step is detailed in its corresponding section in the methods. In summary, the median filter was set with a kernel size of 9×9 pixels, and the histogram equalization with a bell-shaped function with an alpha of 0.5

(Rayleigh distribution). The scale-space for discrete multiresolution analysis was constructed with three octaves and five levels per octave. The threshold of Hessian determinant to define the regions of interest from candidates was 500. For the AdaBoost model, the ensemble of weak learners was constructed using decision trees in 100 iterations. And, for the SVM model with linear and radial base kernels, the parameters were set as default. Code for reproducing the reported results is available at https://github.com/jaruanob/PancreaticCancerDetection-EUS.git.

3.2. Evaluation and results

The performance of the proposed approach was evaluated under a random subsampling cross-validation scheme and was compared with three different typical Convolutional Neural Networks (CNN).

3.2.1. Experimental setup

For the classification task, (a) an AdaBoost classifier was trained with an ensemble of decision trees during 100 iterations, while the SVM classifier used either (b) RBF, and (c) Linear kernels. The trained models perform a binary classification per frame, being pancreatic cancer the positive class and healthy pancreas, liver, gallbladder, or pancreatitis, the negative class. The evaluation included the computation of True Positives (TP), True Negatives (TN), False Positives (FP), and False Negatives (FN). Subsequently, using these values, six metrics were calculated: Accuracy (Acc), Sensitivity (Sens), Specificity (Spec), Positive Predictive Value (PPV) or precision, Negative Predictive Value (NPV), and F-measure (F), as shown in Table **3-1**.

Metric	Description	Equation
Accuracy	Rate of correctly classified frames and the total frames	$\frac{TP+TN}{TP+TN+FP+FN} * 100$
Sensitivity	Proportion of correctly classified frames of a specific class	$\frac{TP}{TP+FN} * 100$
Specificity	Rate of correctly classified frames of other classes	$\frac{TN}{TN+FP} * 100$
Precision	Predictive power to classify a specific class	$\frac{TP}{TP+FP} * 100$
NPV	Predictive power to classify other classes	$\frac{TN}{TN+FN} * 100$
F-score	Weighted combination of precision and sensitivity	$\frac{TP}{TP+\frac{1}{2}(FP+FN)} * 100$

Table 3-1.: Metrics to evaluate the performance of the models.

Random subsampling validation process

A 70-30 validation scheme was applied 10 times to two different databases, i.e., 70 % (≈ 39 cases) was used for training and 30 % (≈ 16 cases) for testing. The two databases are configured as follows:

- *Unbalanced dataset*: the original dataset contains approximately 25 % of frames assigned to the positive class.

- *Balanced dataset:* the original dataset was randomly subsampled to obtain a similar number of frames for each class.

Finally, feature selection explained in section 3.1.2 was applied only to the training set at each of the ten iterations, as explained below. In summary, a feature vector of 256 dimensions consists of the median of 64 features from groups of the scales 2 to 5. Such feature vector is used to train and test the three classification models below.

3.2.2. Results of the random subsampling validation process

According to the experimental setup, the results of the three classification models with the two databases are shown in Table **3-2**. In general, results show this configuration (feature median from groups of scales 2 to 5) discriminates between the two classes using the three classifiers. However, sensitivity and accuracy increased using balanced data, while specificity decreased. The best performance was achieved by the SVM classifier with RBF kernel, i.e., the average accuracy of 92.1 %, sensitivity of 96.3 %, specificity of 87.8 %, and F-measure of 92.4 %. Additionally, the Receiver Operating Characteristic (ROC) curves of the three classification models, as observed in Figure **3-8**, show an Area Under the ROC Curve (AUC) greater than 93.7 %. Detection of small masses is however of particular interest, and in this case the two smaller masses ($22 \times 18mm$ and $20 \times 20mm$) were detected in the sequence of frames with a sensitivity of 94.4 % and 87.9 % by the best configuration (SVM Classifier with RBF kernel).

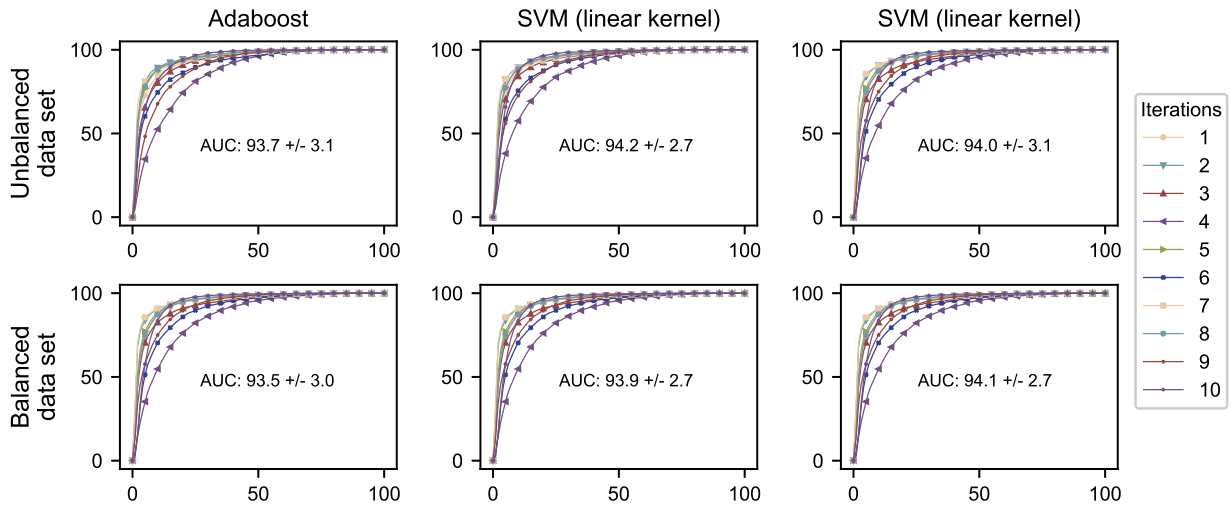

Figure 3-8.: ROC curves for each classification model (columns) using unbalanced and balanced datasets (rows). The X-axis and Y-axis correspond to TP and FP rates (%), respectively. Each graph shows the ROC curves for the random subsampling validation process (10 iterations) and the average AUC.

Few cases showed mislabeled frames, False-negative, and three cases with sensitivity under 80 %, i.e., 67.4 %, 68.4 %, and 74.9 %. Figure **3-9** shows a mislabeled frame from each of these cases, indicating the lesion with a red arrow. The left panel belongs to a video in which the tumor is rarely visible, contaminated by typical transducer reverberation (green arrow). In the mid panel, the echo patterns of a small lesion ($25 \times 25mm$) are blurred by abrupt exploration movements. Finally, in the right panel, a rare tumor is observed, basically as isoechoic patterns, very far from the typical hypoechoic patterns in the database. These three cases, quite far from distinctive tumoral echo patterns, were misclassified. It is worthy to mention that none of the state of the art methods was capable of correctly classify the patterns of right and left images in Figure **3-9**, indicating the number of examples is still very small.

Distribution of classes	**Classifier**	**Acc**(%)	**Sens**(%)	**Spec**(%)	**PPV** (%)	**NPV** (%)	**F-measure**(%)
Unbalanced classes (25 % PC / 75 % non-PC)	*SVM (linear kernel)*	90.6±3.8	89.1±5.1	91.1±4.6	77.9±9.2	96.2 ± 1.8	82.8±6.3
	SVM (RBF kernel)	90.6±3.6	88.6±6.9	91.3±3.6	77.9±7.9	96.0 ± 2.3	82.7±6.5
	AdaBoost	90.4±3.4	87.0±5.9	91.5±3.8	78.1±8.0	95.5 ± 2.0	82.1±5.9
Balanced classes (50 % for each class)	*SVM (linear kernel)*	91.7±2.7	97.1±1.9	86.2±5.3	87.9±3.9	96.8 ± 2.1	92.2±2.3
	SVM (RBF kernel)	92.1±2.7	96.3±2.4	87.8±4.5	89.0±3.6	95.9 ± 2.6	92.4±2.5
	AdaBoost	91.9±2.7	96.1±2.4	87.6±5.9	88.9±4.3	95.8 ± 2.4	92.3±2.3

Table 3-2.: Classification results using the best configuration of the proposed approach.

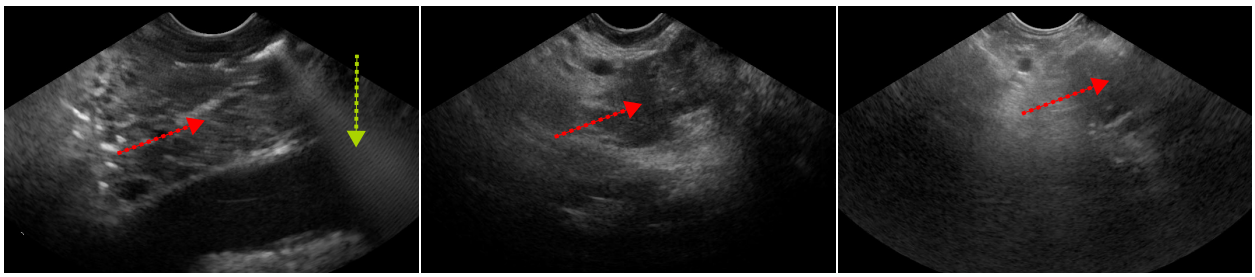

Figure 3-9.: Three different cases with the presence of Pancreatic Cancer were misclassified in some frames. The red arrows show the location of lesions by the expert. The strategy misled when the lesion was partially visible (left image), unfocused echo patterns caused by abrupt movements (center), and an unusual pancreatic tumor showing isoechoic patterns (right).

Comparison with convolutional neural network-based strategies

The proposed approach was compared with three Convolutional Neural Network architectures typically used for EUS image classification tasks, namely GoogleNet, ResNet18, and ResNet50[85, 43, 39, 77]. GoogleNet architecture has been used to detect masses in different organs[43]. While the ResNet architecture has been applied to differentiate pancreatic cancer from pancreatitis or normal pancreas[39] or to detect organs or stages during the EUS procedure[85]. The networks were initialized with pre-trained weights and adjusted following a transfer learning scheme[61]. Each network was configured with the following parameters:

- A Stochastic Gradient Descent as optimizer.
- The loss function is Cross-Entropy.
- A exponential decay strategy to decrease the learning rate during the training.

A grid search process was applied for each network to find the optimal values of four hyperparameters in 30 trials, such as: initial learning rate, batch size, multiplicative factor, and step size of the learning rate decay strategy[1]. The networks were challenged with the same iterations of the random subsampling validation process applied to the proposed approach and using a balanced dataset to avoid overfitting. Additionally, $\sim$9 % of the training data is separated to validate the networks at each epoch. The best model for each network was chosen as the model with the highest validation accuracy along 40 epochs. Then, the selected model was evaluated with the test set. The best configuration of the proposed method is described at the end of section 3.2.1 was used to compare. Results are shown in Table **3-3**.

The proposed approach outperformed the networks in two metrics, with the highest average sensitivity, 96.3 %, to differentiate PC from control. The baseline approaches achieved average specificity of 89.4 %, a value slightly higher than the 87.8 % obtained by the presented

approach. In general, the method outperformed the others to detect the negative and positive classes, reaching 92.1 % of average accuracy.

Strategy	Configuration	Acc(%)	Sens(%)	Spec(%)	PPV(%)	NPV(%)	F-measure(%)
Proposed approach	*Median of features from 4 scales + SVM (RBF kernel)*	92.1±2.7	96.3±2.4	87.8±4.5	89.0±3.6	95.9 ± 2.6	92.4±2.5
Deep learning-based frameworks	*GoogleNet (Liu et al.[43])*	87.2±4.1	85.0±8.2	89.4±6.2	86.8±4.7	86.1 ± 6.0	89.4±5.2
	ResNet18 (Liu et al.[43])	85.6±4.2	81.8±10.1	89.4±6.9	84.8±5.2	83.8 ± 6.7	89.3±5.5
	ResNet50 (Kuwahara et al.[39])	90.0±3.0	86.9±6.0	93.0±3.8	89.6±3.4	87.9 ± 4.7	92.8±3.5

Table 3-3.: Comparison between the proposed approach with three deep learning strategies under the same validation process.

Evaluation with images corrupted by white and speckle noise

Multiplicative noise is always present in EUS images, specifically the Speckle Noise. Also, US images are perturbed by stochastic noises such as White Noise. Both noises are exacerbated by the device maneuver during EUS exploration, distorting the tissues and difficulting the detection of masses or pathologies. This condition was simulated by corrupting the testing set with speckle noise (1, 10, 20, and 30 %) and white noise (1, 10, 20, and 30 %), and data was also 70-30 partitioned. All methods were firstly evaluated without noise, and the results were similar to the ones presented in section 3.2. Afterward, the noise was applied, as previously mentioned, and the results, in terms of F-measure, are shown in Figure **3-10** (complete data is shown in Annexe C). The proposed method with the three different models maintains almost the same F-measure as the observed without noise, independently of the added noise level. Interestingly, the networks were strongly affected, and their performance decreased. While proposed models maintain the F-measure above 94 % for the different levels of Speckle Noise, the ResNet50 falls down to 65 %, and the GoogleNet keeps about 90 %. Notice that the performance is also decreased when white noise is added, and sometimes the pattern is quite erratic, i.e., the ResNet50 falls down for 10 % of noise, but then the performance improves a little bit with higher noise proportions. However, the performance of the nets is always lower than the machine learning models.

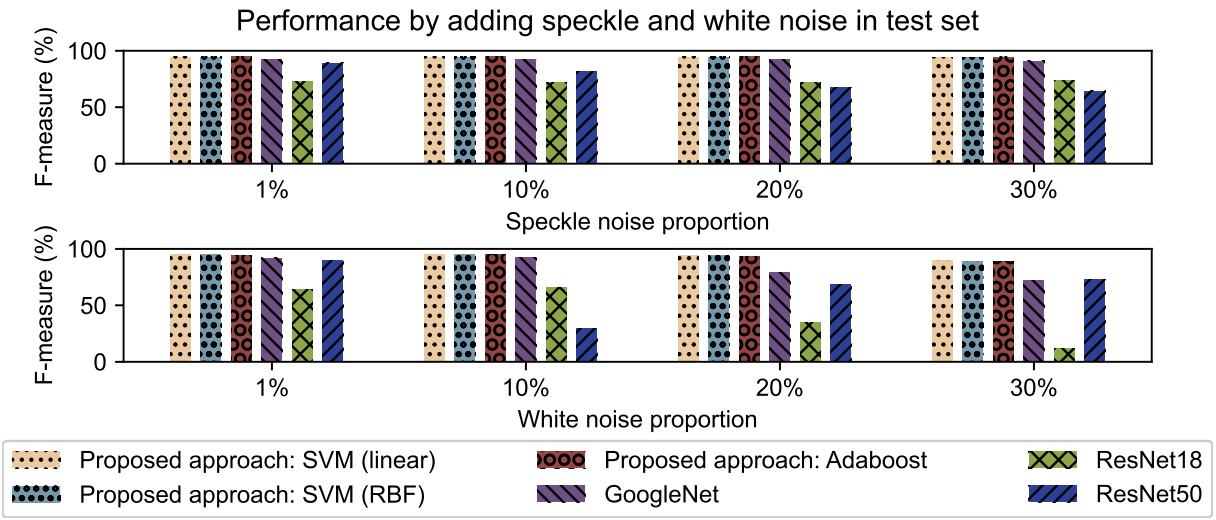

Figure 3-10.: Performance (F-measure) of the proposed method and the baseline strategies when the test set is contaminated with speckle (up) and white (down) noise in different proportions. Proposed models maintain the F-measure above 94 %, independly of noise levels. However, the performance of the nets is always lower than the machine learning models. The ResNet50 falls down to 65 %, and the GoogleNet keeps about 90 %. Sometimes the pattern is quite erratic, i.e., the ResNet50 falls down for 10 % of noise, but then the performance improves a little bit with higher noise proportions.

3.3. Discussion

This work introduces a second reader of pancreatic cancer (PC) in Endoscopy Ultrasonography (EUS) videos by detecting frames with tumoral pancreatic masses. Although computational tools have been developed as second readers for EUS procedures, they have addressed limited scenarios. Usually, they are semiautomatic and identify between PC, CP, or NP in pre-selected EUS images or Regions of Interest (RoI)[85, 86, 63]. For instance, Zhang et al.[86] differentiate PC and non-PC patches extracted from a collection of EUS images composed of 216 cases diagnosed by two gastroenterologists. Of the cases, 153 were confirmed with PC by histopathology analysis. The remaining 63 cases include patients with NP and CP. For each case was selected a single frame, and the tumoral region was delineated by a specialist to extract RoIs. Inside regions of the lesion was defined as tumoral RoIs. While, the rest of the frame was defined as non-tumoral RoIs. This choice implies that the same type of noise is present for the positive and negative classes, and an inevitable bias that was avoided in the present investigation by including different frames and cases in the negative class. After the region was pre-selected, a histogram of the pixel intensities was computed from each RoI to extract a set of fractal features of the M-band wavelet transform. Such

representation was used to feed an SVM classifier, obtaining 97.98 % of accuracy under a validation scheme of 50 random partitions between the training and testing sets. Similarly, Zhu et al.[87] developed a strategy using frames and RoIs selected by an expert. But, in this case the PC samples were differentiated from CP using 262 and 126 EUS images for each class, respectively. A total of 105 statistics were computed for each RoI from the gray-level histogram and the wavelet transformation, ending up with 25 statistics selected by the Sequential Forward Selection algorithm. An SVM classifier was trained over 200 trials of randomized experiments, obtaining an accuracy of 94.2 % and specificity of 96.25 %. Although these methods obtained good results, the influence of expert assistance was not determined. Likewise, as previously mentioned, positive and negative regions come from the same frame and therefore the noise is similar, a remarkable reduction of variance since ultrasound is well known for the capturing multiplicative noise[47]. This is not only a limitation of this experimental setup but also an intrinsic weakness of most deep learning approaches, which have been reported to be quite sensitive to noise[42]. In addition, the wavelet analysis applied by both works is not rotation invariant and probably might not capture the heterogeneous patterns of the tumor regions at different orientations as usually occurs in a complete exploration. In contrast, the method herein proposed identifies which frames may contain a PC along a complete EUS video sequence without any expert intervention, while the SURF wavelet analysis was aligned by the dominant orientation of the interest points, capturing diverse patterns and preserving the description regardless of the view.

Deep learning-based frameworks have been applied to classify ultrasound images in different organs, i.e. Liu et al.[43] and Kuwahara et al.[38] with the GoogleNet architecture. Tonozuka et al.[77] designed a small CNN to classify PC and non-PC cases from manually selected images of 139 EUS videos. This network assembled 6 blocks for feature extraction, each containing convolution, normalization, and activation layers, and 4 max-pooling layers which downsize the features maps. At the end of the network, a convolutional layer obtained a score map with a probability of each position to be one of the two classes. The classification task reported 92.4 % of sensitivity and 84.1 % of specificity, yet remarkable results, the strategy performance depends on expert selection. In contrast, the method herein proposed is fully automatic and detects PC frame-by-frame, with a sensitivity and specificity of 96.3 %, and 87.8 % respectively. On the other hand, Kuwahara et al.[39] developed a strategy to predict whether precursor lesions of PC or Intraductal papillary mucinous neoplasms (IPMNs) are malign or benign. The CNN architecture used was the classical but still competitive ResNet50 as the feature extractor, followed by a Global average classification layer. This network was fed with 508,160 images produced by the data augmentation process from 3,970 EUS images, recorded from 50 patients diagnosed with IPMN. Performance was evaluated under a 10 fold-cross-validation scheme, reporting a 95.7 % of sensitivity, 92.6 % of specificity, and accuracy of 94.0 %. In contrast to previous works, this method used frames from a small temporal interval of the EUS video. Nevertheless, these authors did not analyze a complete exploration of the pancreas, or a differential diagnosis challenge, i.e., pancreatitis cases. To compare

with these deep learning-based frameworks (see section 3.2.2), two optimized versions of ResNet and GoogleNet networks were tested with the collection of videos used in this work. The ResNet50 architecture reached 90.0 % of average accuracy, 86.9 % of sensitivity, and 93.0 % of specificity. In contrast, the method herein presented, computationally much less expensive, showed higher averaged accuracy (92.1 %), a sensitivity of 96.3 %, and a precision of 92.4 %. Additionally, these networks were very sensitive to typical noises when the testing set was contaminated with either white or speckle noise at different percentages (see section 3.2.2). In the case of white noise, uncorrelated at different scales, the proposed approach was more robust, obtaining an F-measure above 88 %. In the case of speckle noise, the proposed method, independently of the added noise level, obtained an F-measure above 94 %, while the ResNet50 network hardly reached a 65 % of F-measure when speckle noise was 30 %.
The proposed method outperformed state of the art neural networks, likely because this strategy characterizes relevant texture patterns by a feature adjusted multi-scale descriptor. In addition, this method is robust to noise, an acknowledged limitation in the case of neural networks that have a strong data dependency and may overfit, which looks the case here. Furthermore, the actual applicability of deep learning methods is at least complicated because these models require constant re-training in a problem with few data. The presented method also showed limitations, mainly related with the number of examples for particular conditions, precisely certain types of rare tumors, hidden lesions that demand more abrupt maneuvers of the gastroenterologist, and partially visible lesions. Nevertheless, the performance of the method was remarkable, with specificity above 90 %. Finally, the current method implementation in MATLAB is not optimized, and yet the average execution time to process a frame in the whole database (66,249 frames) using a regular laptop (Intel Core i7 with 4 cores running at 2.20 GHz and 8 GB of RAM) was 0.465 $\pm$ 0.028 seconds per frame.
Other methods have focused on using EUS elastography and contrast-enhanced techniques, to characterize PC. Saftoiu et al.[64, 63] applied a multi-layer perceptron to classify EUS using any of these features. In the former case[64], the network was fed by features of the hue histogram, reporting an average accuracy of 95 %. In the latter case[63], the contrast-enhanced EUS histogram was reported to obtain a sensitivity of 94.64 % and specificity of 94.44 %. However, multi-center evaluation has shown elastography is highly dependent on the force the specialist applies to the intestinal wall, i.e., a constant endoscope force during an actual maneuver is hardly reproducible[41]. On the other hand, the contrast-enhanced EUS procedure requires intravenous contrast agent injection, reason why this is not routinely used in endoscopy exams.

3.4. Conclusions

The proposed approach detects pancreatic cancer during video endoscopic ultrasonography procedures. The method outperformed state of the art methods at identifying frames with

and without tumors, even in simulated noisy conditions, while data dependence is remarkably lower. In addition, the method does not require a pre-selection of potentially suspicious frames, i.e., the strategy is able to deal with a complete exploration of multiple organs and the typical noisy conditions throughout a complete video, making this methodology more real application. The strategy may be used as a guide for interns during training, i.e., while they learn to interpret the anatomy of the pancreas, they may also learn the echo patterns associated with lesions. This guidance would speed up the learning process of trainees, incrementally improving their lesion identification. Likewise, the methodology does not require a specific configuration of the ultrasound device since the method was developed with a typical configuration, being easy to use and get started. In contrast, for the experts, the tool may be a trustworthy second reader, as demonstrated by the collection of cases herein evaluated.

The cases[33] and implementation[60] used in this work are publicly available. Although the proposed method is not significantly expensive in computational terms, future work includes developing a real-time application to be used in clinical practice by migrating the current implementation to compiled programming languages. In addition, to feed the database with pancreatitis cases and exceptional situations such as those producing false negatives

4. Complementary evaluation of Deep Learning approaches in echoendoscopy videos

This chapter shows an additional experimentation of the Deep Learning approaches used to compare the methodology of section 3. Herein is presented a procedure to capture the previously mentioned heterogeneous EUS patterns based on a deep learning approach, adapting pre-trained nets to the EUS domain by a transfer learning strategy. Such characterization is performed frame-by-frame using classical architectures such as ResNet and GoogleNet. Therefore, two methodologies are presented to differentiate pancreatic cancer in complete sequences of frames. First, in section 4.1, the nets are trained to solve a binary problem, differentiating frames between pancreatic cancer and non-pancreatic cancer. Also, the nets are trained using optimized hyperparameters, and the impact of the pre+postprocessing step is evaluated. Moreover, the impact of introduced noises is evaluated. Second, in section 4.2, the ResNet50 was selected to solve a multiclass problem, differentiating frames between pancreatic cancer, pancreatitis, and healthy pancreas.

4.1. Automatic detection of PC using deep learning framework

This subsection is based on the article "Automatic detection of pancreatic tumors in endoscopic ultrasound videos using deep learning techniques"[34] presented to participate at Medical Imaging 2022 of SPIE, accepted for oral presentation, and published on the SPIE platform.
Abstract: *Pancreatic Cancer (PC) is one of the most aggressive cancers, with a mortality rate of 98 %. Although the diagnosis of PC is difficult in early stages, several imaging techniques support the screening process, i.e., ultrasonography (US), computed tomography (CT), and endoscopic ultrasound (EUS). EUS procedure reports the highest sensitivity (up to 87 %), and histological samples may be acquired during the same procedure. However, EUS sensitivity depends on the gastroenterologist's experience. The presented method performs an automatic frame-by-frame detection of PC in complete EUS videos. First, the images are preprocessed to rearrange the radial image intensities, filter out the Speckle Noise, and perform a contrast enhancement to highlight relevant echo patterns. Then, a pre-trained Convolutional*

Neural Network (CNN) is adapted to the ultrasound domain by a transfer learning strategy to characterize and classify EUS images between PC and non-PC classes. Finally, mislabeled images are corrected by a temporal analysis. The methodology is evaluated using a dataset of 66,249 frames from 55 EUS cases. In total, 18 patients are labeled as PC class, and 37 are labeled as non-PC class. A cross-validation scheme is applied seven times to evaluate the performance of three convolutional neural networks: GoogleNet, ResNet18, and ResNet50 architectures. The best results were 93.2±4.0, 87.7±5.4, 95.0±5.6, and 87.0±6.7 in accuracy, sensitivity, specificity, and F-score, achieved with the ResNet50 architecture.

4.1.1. Methodology

Tissues in Ultrasound images are characterized by their Echogenicity, which is the ability to reflect or transmit the US waves depending on the tissue composition[30, 56]. Typically, a tumoral zone is characterized by a complex mixture of hyperechoic, hypoechoic or anechoic patterns, in contrast with healthy tissues that present well-defined areas of echo patterns[56]. This work characterizes the variability of the echo patterns extracted from complete videos of Echoendoscopy (EUS) procedures. First, a preprocessing step is applied to rearrange the radial distributed intensities, filter out the Speckle Noise, and highlight the echo patterns. This process is shown in section 2.1.6. Then, EUS images are characterized by a transfer learning strategy, adapting a pre-trained convolutional neural network from natural images to the EUS domain. The adapted fully-connected layers classify a frame between pancreatic cancer and non-pancreatic cancer. Subsequently, a temporal correction strategy filters out the misclassified frames in a specific temporal window. Finally, this process is applied frame-by-frame during a video, detecting the presence of pancreatic cancer (PC). The pipeline of this methodology is shown in Figure **4-1**

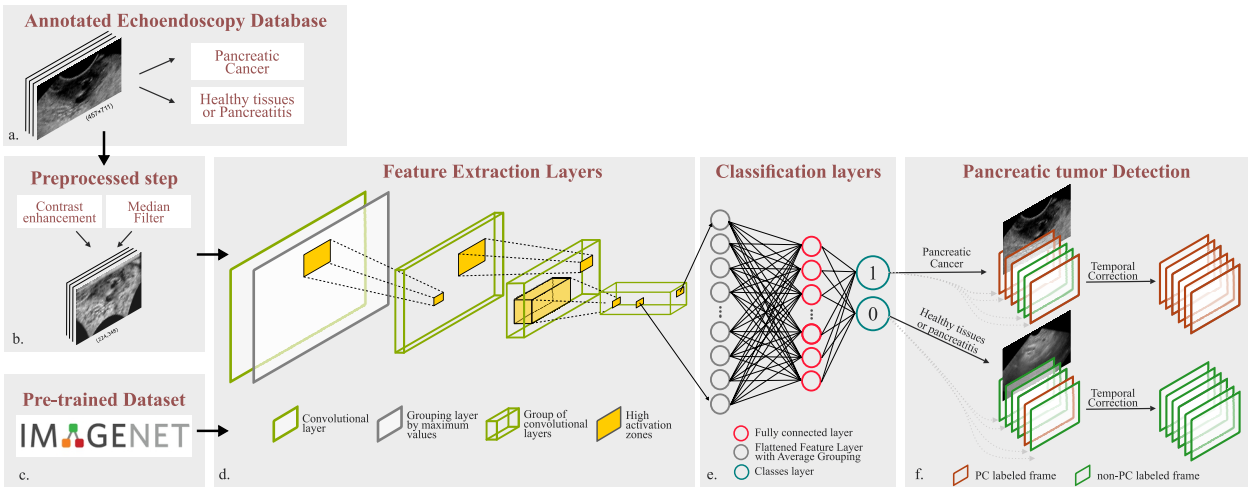

Figure 4-1.: Proposed method pipeline. First, a frame-by-frame annotated database of endoscopy videos is divided into PC class and non-PC class(a), and a preprocessing step is applied(b). Then, a convolutional neural network is pre-trained with millions of natural images and (c) adjusted to the ultrasound domain using the transfer learning strategy (d). Finally, the trained network is evaluated (e-f) to detect frames with pancreatic tumors.

Convolutional neural network architectures

Heterogeneous patterns of tumoral zones in EUS images may be characterized using a convolutional neural network (CNN). The CNN builds a hierarchical representation of the distinctive echo patterns to detect frames with pancreatic cancer in complete EUS videos. A CNN is a set of layers sequentially connected, each layer composed of neurons that are grouped to estimate task-dependent filters. The first layers convolve the filters with the input EUS image, decomposing them to basic visual concepts, primitives, or local patterns. Then, the resulting decomposition is progressively convolved with subsequent layers to compress the information. Although CNN is a data-driven method, many classical architectures have been extensively trained and validated in natural images, using databases with millions of images, such as the ImageNet database[15, 61]. The natural domain represents a wide range of local and global patterns that could be adapted to other domains, such as the EUS domain. A transfer learning strategy adapts the domain by adjusting some layers of the network with an iterative-adaptive process using a relatively low learning rate along the epochs.

In this work, three classical net architectures pre-trained with the Imagenet database are used: GoogleNet, ResNet18, and ResNet50. The convolutional layers are frozen and used as feature extractors. The fully connected layers are adapted and trained to differentiate frames between positive or PC class (pancreatic cancer) and negative or non-PC class (healthy tissues of the pancreas, liver, gallbladder, other gastrointestinal tumors, and pancreatitis). This process is shown in Figure **4-1.d-e**. A description of these architectures is presented

below.

- **Googlenet:** architecture of 22-layers, composed of 9 Inception Modules and $\sim 7M$ parameters. These modules first concatenate a filter of size 1×1 to reduce the network parameters and perform a rectified activation before the expensive 3×3 and 5×5 filters. This process decreases the number of operations and builds deeper networks without the significant computational overhead. This architecture won the ImageNet Large Scale Visual Recognition Contest (ILSVRC) in 2014 for image classification and object detection[75, 61]. This net has been applied to breast cancer diagnosis in US images[43].

- **ResNet:** Architecture incorporates direct connections between non-contiguous layers, reducing the problem of gradient attenuation in deeper layers, creating the so-called residual blocks. These connections improve the performance of the classification tasks, training deeper networks. One version of this network won the ImageNet Large Scale Visual Recognition Contest (ILSVRC) in 2015 [23]. The number of trainable parameters of ResNet18 and ResNet50 is 11M and 23M, respectively. This architecture is used in US images from different organs: in the heart to recognize cardiac cycle phases, in the prostate to delineate the gland[43], and in the pancreas to predict malignancy in intraductal papillary mucinous neoplasms[38].

Temporal correction

A temporal vector is constructed by collecting the predicted labels per frame in the classification stage. Inside this vector, misclassified frames are filtered out by approximating a stationary stochastic process within a moving window. Each frame is binarily labeled: when a frame contains a tumor is set as one. Otherwise, the frame is set as zero. A regression is applied using the labels in a predefined window. The model predicts the value of a frame using the information present in the window: if more than a threshold of the frames is one, the frame is labeled as the positive class. This process is shown in Figure **4-2**. In this work is defined a window size of 61 frames, and the threshold is set to 25 %

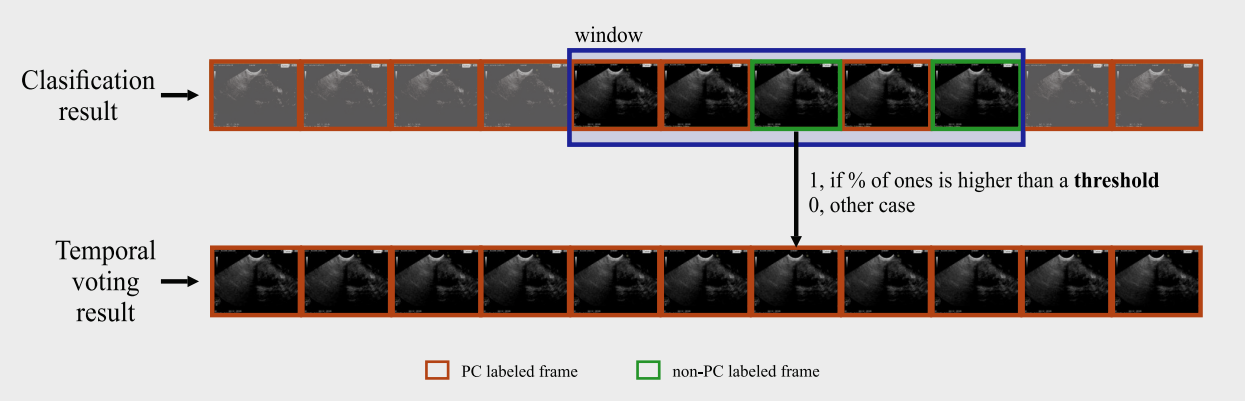

Figure 4-2.: Temporal correction of misclassified frames: if the number of labeled frames within a window are larger than a threshold, the frame is labeled as positive.

4.1.2. Results

The proposed methodology is assessed using the dataset detailed in chapter 2. In total, 66,249 frames are classified, 16,585 are positive class, and 49,664 are negative class. The methodology performance is evaluated by comparing the predicted label of each frame with the annotation by the experienced gastroenterologist. Also, the performance of three net architectures is assessed (ResNet18, ResNet50, and GoogleNet). The experimental setup, quantitative validation, and qualitative results are presented below.

Experimental Setup

Cross-validation scheme

The method is evaluated under a cross-validation scheme of 7 iterations. At each iteration, ~ 38 cases are used for training and ~ 17 for testing. Additionally, ~ 4 cases of the training set are used to validate the networks at each epoch. However, the dataset is unbalanced between PC and non-PC cases, and each respective number of frames, i.e., the training set is composed of $\sim 46,638 \pm 114$ frames distributed in $\sim 11,660 \pm 22$ frames with PC and $\sim 34,978 \pm 106$ without PC. Since the networks are susceptible to overfitting in unbalanced datasets, two strategies are evaluated to balance the number of frames between classes. Additionally, the nets are trained and tested with two image types: preprocessed images according to section 2.1.6 and original images from the database to evaluate the impact of the preprocessing stage on the performance of nets. Hence, each architecture is evaluated using the following database configurations:

- ***Subsampled+original*:** The database is balanced with respect to the number of frames from the PC class ($\sim 11,660 \pm 22$), i.e., approximately two-thirds of the non-PC class frames are randomly removed, obtaining a total of $\sim 11,691 \pm 81$ frames. Also,

the nets are trained with the raw images of the database (without the preprocessing step).

- ***Augmented+original*:** In this case, the database is balanced with respect to the number of frames from the non-PC class ($\sim 34,978 \pm 106$) using a data augmentation strategy. This technique creates synthetic images of the PC class, applying flip, zoom, and combination of both operations in random frames to achieve $\sim 39,058 \pm 2,303$ frames in the PC class. Additionally, pancreatitis frames from the non-PC class are augmented twice following the previous augmentation policies to obtain $\sim 39,843 \pm 1,706$ non-PC frames. Also, the nets are trained with the original images of the database.

- ***Augmented+preprocessed*:** The nets are trained using the augmented dataset shown in the previous configuration. But, in this case, the preprocessing step is applied to the input images. Additionally, the images are resized using two image resolutions: the original size of the database (457×711 pixels) and a similar size of the network configuration (224×348 pixels).

The unbalanced proportion of data is preserved in the testing stage. The strategies are tested using the unbalanced dataset of $\sim 19,611 \pm 114$ frames, in which 25 % of the data corresponds to PC-class and 75 % to non-PC class.

Hyperparameters of networks and optimization

The selected convolutional neural network architectures are GoggleNet, ResNet18, and ResNet50, initialized with pre-trained weights from the ImageNet database. The loss function is cross-entropy, and the optimization algorithm is stochastic gradient descent. The learning rate during the training stage is reduced using the exponential reduction strategy, configured with a reduction factor at every epoch.
Additionally, a grid search strategy is used to maximize the accuracy, looking for an optimal combination of 5 hyperparameters: a) initial learning rate, b) batch size, c) decay factor of the weights, d) the factor, and e) the number of epochs of the learning rate reduction strategy [1]. This optimization process is carried out throughout 30 trials, using 25 % of the training data at each iteration in the subsampled dataset. However, this process is applied 20 times with 10 % of the training data in the augmented dataset to reduce the extensive training time. Subsequently, the nets are trained using the complete dataset with the best hyperparameter configuration found in the previous process. Finally, the testing dataset is evaluated using the model with the highest validation accuracy over 40 epochs.

Performance Metrics

The convolutional neural network predicts a label between non-PC and PC classes. Network performance is quantified by comparing the predicted label for each frame with the expert

annotation. This comparison is consolidated in a confusion matrix to obtain: a) True Positives (TP), b) True Negatives (TN), c) False Positives (FP), and d) False Negatives (FN). Subsequently, five metrics are calculated using the confusion matrix: accuracy, sensitivity, specificity, precision, and F1 score.

Quantitative Results

Cross-validation evaluation

Performance metrics are shown in Table **4-1**, which is composed of three blocks to compare the results of each configuration explained in Section 4.1.2. The first block presents the *subsampled+original configuration*. The best result was obtained by the ResNet50, with an accuracy, sensitivity, and specificity of 92.2±4.8, 94.6±2.2, and 91.3±6.2, respectively. Then, the results of *augmented+original* configuration are shown in the second block, achieving the best performance throughout all experiments with accuracy and specificity of 93.2±4.0 and 95.0±5.6, respectively, using the ResNet50 architecture. Finally, the third block shows the results of *augmented+preprocessed* configuration. The ResNet50 also the architecture with the highest results with an accuracy and specificity of 89.8±5.9 and 92.3±6.8, respectively, using images with the original size. In the case of rescaled images, although the method achieved lower results, the ResNet18 architecture reached 92.2±6.2 of sensitivity.

In general, the increased variability of the input images in the augmented database improves the generalizability of the models, achieving better results in terms of accuracy and F-score. Also, in terms of architectures, the results of ResNet and GoogleNet architectures are equivalent, achieving an F-score and accuracy higher than 76 % and 87 %, respectively. Both models were able to describe and differentiate remarkably the high variability of normal tissue and pancreatitis and the mixture of textural patterns of pancreatic cancer. Nevertheless, GoogleNet architecture is the smaller network with 4M and 16M fewer trainable parameters compared to ResNet18 and ResNet50, respectively, being the net with the lowest computation cost. Finally, although the performance of the nets slightly decreased using the preprocessing step, the generalizability of the method is higher, as shown in section 4.1.3.

Configuration	Input size	Network	Acc(%)	Sens(%)	Spec(%)	Prec(%)	F1(%)
Subsampled +original	457×711	*GoogleNet*	88.7±6.5	93.0±4.1	87.2±8.6	72.9±12.2	81.2±8.4
		ResNet18	88.1±6.8	91.1±6.3	87.1±9.7	73.0±13.3	80.2±8.4
		ResNet50	**92.2±4.8**	**94.6±2.2**	**91.3±6.2**	**80.0±11.6**	**86.3±7.3**
Augmented +original	457×711	*GoogleNet*	91.3±4.7	86.7±5.0	92.8±5.7	81.7±12.2	83.7±7.6
		ResNet18	90.9±5.8	**88.4±7.5**	91.7±7.8	80.6±13.2	83.6±8.3
		ResNet50	**93.2±4.0**	87.7±5.4	**95.0±5.6**	**87.4±12.4**	**87.0±6.7**
Augmented +preprocessed	224×348	*GoogleNet*	88.0±6.7	87.0±7.3	88.3±8.2	73.4±13.9	79.1±10.0
		ResNet18	89.7±5.7	**92.2±6.2**	88.8±7.1	75.0±12.3	**82.3±8.6**
		ResNet50	89.5±6.4	88.7±8.3	89.7±8.7	77.2±15.1	81.7±9.7
	457×711	*GoogleNet*	87.9±5.4	86.0±10.9	88.6±6.4	72.8±10.8	78.4±9.0
		ResNet18	87.9±6.0	78.7±11.6	91.0±6.5	76.2±13.5	76.8±10.7
		ResNet50	**89.8±5.9**	82.3±10.8	**92.3±6.8**	**80.4±14.3**	80.6±10.3

Table 4-1.: Comparison of the performance of the nets with both balanced datasets and the preprocessing step.

Qualitative Results

Examples of True-positives, True-negatives, False-positives, and False-negatives predictions from the best configuration obtained by the method are shown in Figure **4-3**, i.e., ResNet50 architecture using the original image and the augmented dataset.

PC class examples are shown in the first and second columns of Figure **4-3**. The method manages the high variability of tumoral shape and heterogeneous echo patterns, as shown in true-positive samples. The worst cases of PC class are C13 and C18. First, the C13 case has the smaller lesion of the database(2×2cm). Therefore, the tumor is visualized as very small and without heterogeneous textures. Besides, the C18 case has low contrast, and the tumor has a hypoechoic pattern without heterogeneous textures.

Non-PC class examples are shown in the third and fourth columns of Figure **4-3**. This class is composed of frames with different kinds of tissues, as displayed in Figure **4-3** with arrows, such as: pancreas (green), kidney (yellow), liver (blue), and gallbladder(purple). Misclassified frames of this class occur in low contrast images, blurry images, abrupt transducer movements, or images with ring-down and reverberation artifacts. Worst results were achieved in cases with tumors in other organs, such as the H12 case diagnosed with a GIST tumor (Gastrointestinal stromal tumors) and H18 with a Lipoma Tumor.

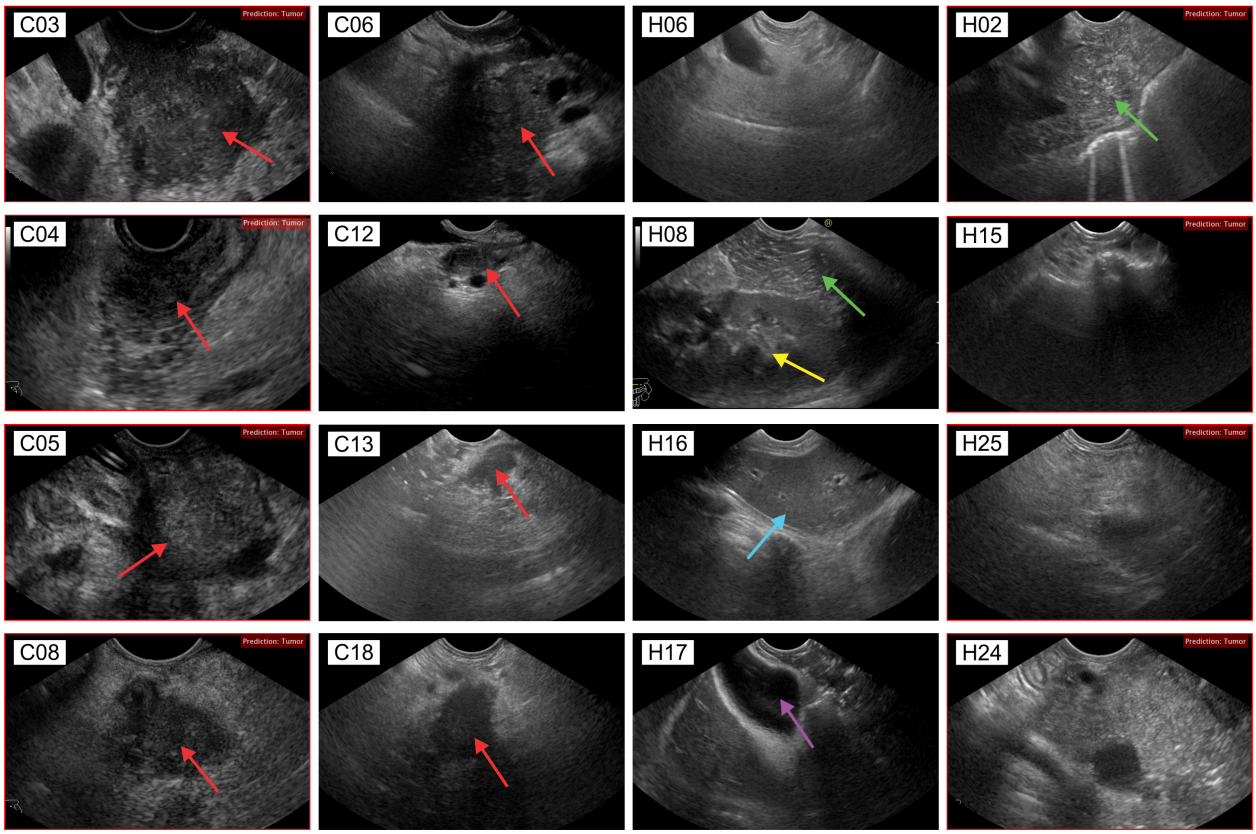

Figure 4-3.: Qualitative Results: each column represents frames labeled as: 1) True Positive, 2) False negative, 3) True negative, and 4) False positive. Arrows in the images represent: tumors (red), healthy pancreas (green), liver(blue), kidney (yellow), and gallbladder (purple).

4.1.3. Evaluation with images corrupted by speckle and white noise

Typically, US images are contaminated by speckle or white noise, limiting the detection of injuries, especially in low contrast images[47]. These noises depend on different factors such as the device configuration, abrupt movements, and angle of incidence with the tissues. Therefore, the benefit of including the preprocessing and temporal correction (pre+post-processing) steps in the CNN-based workflows herein is evaluated, i.e., the nets are challenged with and without the pre+post-processing steps using images corrupted by different levels of noise. However, public databases that include such noisy conditions are not available in the state of the art. Hence, the testing set of the database was contaminated with speckle and white noise using a variance of 1 %, 5 %, and 10 % separately, and the three networks were tested.

The impact of these noises in the nets in terms of F-score is presented in Figure **4-4**. Results demonstrate that the performance of the nets is slightly less affected by the noise when the pre+post-processing steps are applied. E.g., the F-score obtained by ResNet50 without

pre+post-processing decreased dramatically from $\sim 80\,\%$ to $\sim 66\,\%$ in $10\,\%$ of White noise. Meanwhile, the nets with pre+postprocessing almost preserved the same F-score, from $\sim 82\,\%$ to $\sim 80\,\%$. The previous interpretation is similar to the results obtained by RestNet18 in White noise and ResNet50 in Speckle noise. Surprisingly, although GoogleNet is the smallest network evaluated in this work, the obtained F-score was the less impacted, even in $10\,\%$ of Speckle and White noises. In contrast, deeper networks such as the ResNet50 are over-fitted with the training set, and in subtle changes in the testing set, the network was induced to misclassification, as shown in these experiments. Also, the networks trained and tested with small-size images are less affected. Hence, the median filter and contrast enhancement process filter out the Speckle and White noise and highlight the representative echo patterns to be characterized by the network. Also, the temporal voting stage corrects misclassified frames caused by artifacts associated with the device movement.

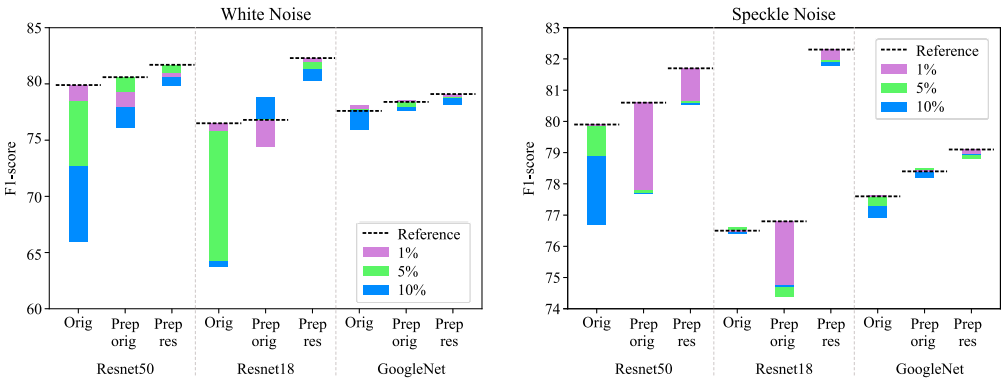

Figure 4-4.: F-score differences between the original and corrupted datasets. The reference is the performance of the nets without noise.

4.1.4. Conclusions

The proposed method achieved outstanding performance to detect pancreatic cancer in images of endoscopic ultrasound procedures. The method was able to handle the high variability of complete videos, differentiating cancer from pancreatitis, healthy pancreas, and other tissues with a remarkable performance. Such variability was not considered in the state of the art methods. Also, it was demonstrated that the performance of the Neural Networks is better when the dataset is balanced by applying augmentation policies. Although the performance of networks trained and tested with preprocessed images is slightly lower, the nets are more robust to Speckle and White noises. Future work includes increasing the number of cases of pancreatic cancer and pancreatitis. Additionally, the method may be challenged in a multi-class problem: pancreatic cancer, pancreatitis, and healthy tissue.

4.2. Classification of a Multiclass problem

This subsection is based in the article "Detección automática de tumores pancreáticos en vídeos de ecoendoscopia usando técnicas de aprendizaje profundo", presented at Congreso de las Asociaciones Colombianas del Aparato Digestivo ACADI 2021, in which the work won the first place of José Jácome Valderrama competition. ***Abstract:*** *Introduction: Pancreatic Cancer has a mortality rate of 98 % (one of the higher rates in cancer). Also, the 5-year survival rate is less than 7 %. In addition, 75 % of cases are diagnosed in advanced stages because PC is an asymptomatic disease in early stages. Several medical image modalities have been used for the diagnosis of pancreatic cancer. However, Endoscopic ultrasound achieves the highest sensitivity in pancreatic cancer detection, and EUS-FNA is used to guide the biopsy acquisition for histopathological confirmation, standing out from other methods. However, endoscopic ultrasound is a highly operator-dependent procedure for the complexity in the anatomical interpretation altered by the typical noise sources in these images and the similarity of other abnormalities such as pancreatitis. Hence, an automatic and robust second reader based on artificial intelligence is desirable to support the detection of pancreatic cancer. Objective: Automatic classification frame-by-frame of endoscopic ultrasound videos to differentiate pancreatic cancer from frames with pancreatitis or normal tissue. Methodology: the proposed approach is based on a deep learning strategy in a convolutional neural network, specifically the ResNet50 architecture. This network is trained under a transfer learning technique, which is initialized with pre-trained weights in millions of natural images, learning to characterize local and global patterns used to describe endoscopic ultrasound frames. Subsequently, the network is adjusted to the ultrasound domain by modifying the classification layers and training the network with endoscopic ultrasound frames. Those frames were previously preprocessed to reorganize and highlight the relevant ultrasound patterns. This approach was evaluated using 55 cases acquired in two different centers, with approximately 38.083 images in total. Results: A random cross-validation scheme was applied with 5 iterations, with partitions of 75 % for training and 25 % for testing. At each iteration, the hyperparameters of the network were optimized based on the grid search technique throughout 20 tests. The predictions made by the method were compared with annotations made by an expert with more than 20 years of experience, obtaining an average accuracy of 79.5 % for frames with normal tissue, 90.1 % with pancreatitis, and 84.3 % for Pancreatic Cancer frames. The global results obtained were an average accuracy, sensitivity, and specificity of 84.8 %, 78.9 %, and 87.7 %. Conclusions: The proposed method achieved outstanding performance to detect pancreatic cancer, being capable of differentiating cases of pancreatitis from pancreatic tumors, and overcoming the high variability of a complete endoscopic ultrasound procedure. Such variability was not considered in the state of the art methods.*

4.2.1. Methodology

In this case, the applied methodology is similar to section 4.1. Preprocessed images are selected to train a ResNet50 architecture, solving a multiclass problem: classify between frames with the presence of Pancreatic Cancer (PC), Chronic pancreatitis (CP), or normal pancreas (NP). The pipeline of this methodology is shown in Figure **4-5**.

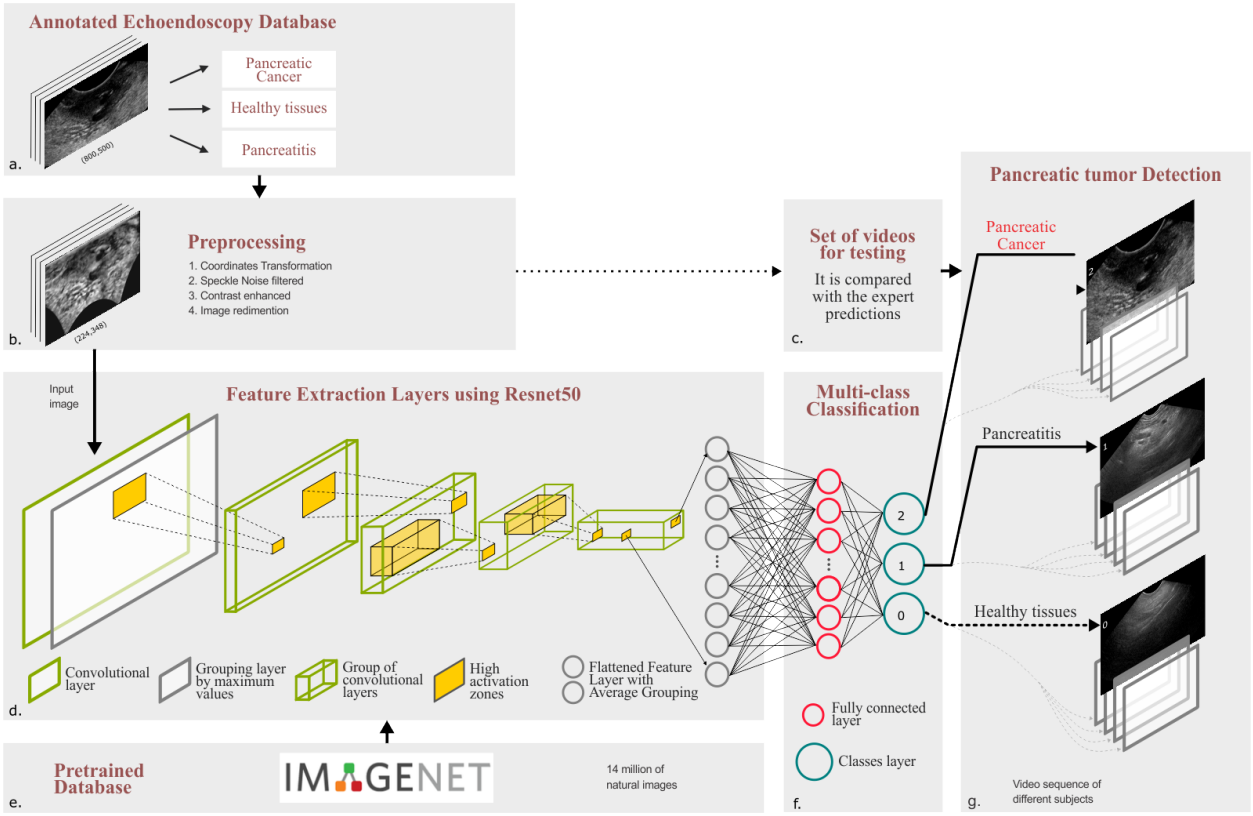

Figure 4-5.: The pipeline of the proposed method to automatically detect pancreatic tumors frame-by-frame in endoscopic ultrasound videos. First, a frame-by-frame annotated database of endoscopy videos was divided into Pancreatic Cancer, Healthy pancreas, and Pancreatitis classes (a). Then, each frame is preprocessed (b), and the dataset is divided into training and testing partitions (c). Afterward, convolutional neural networks are pre-trained with millions of natural images (e) and adjusted to the ultrasound domain using the transfer learning strategy, training only the last layers (d). The trained network is evaluated to differentiate frames between classes(f-g).

4.2.2. Convolutional neural network architecture

As shown in section 4.1, echo patterns could be extracted by a convolutional neural network (CNN) to differentiate pancreatic cancer from normal tissues and pancreatitis. The expla-

nation of Neural Networks architectures is performed in subsection 4.1.1. In this work, the selected architecture was ResNet50[23]. This 50-layer architecture stands out from others since this net incorporates direct connections between non-contiguous layers, reducing the problem of gradient attenuation in the deeper layers, creating the so-called residual block. These connections improved the performance of image classification tasks, training deeper networks than conventional ones. The deepest version of this network won the ImageNet Large Scale Visual Recognition Contest (ILSVRC) in 2015 [15]. The network architecture is described in Table **4-2**.

# of layer	**Class**	**Description**	**Filter size**
1	Convolutional	Receive input image	7 x 7
2	Max Pooling	Reduce dimensionality taking the maximum value	3 x 3
3 to 11	3 x Residual block	Each block have 3 convolutional layers	One block have: 1st layer: 1 x 1 2nd layer: 3 x 3 3rd layer: 1 x 1
12 to 23	4 x Residual block		
24 to 41	6 x Residual block		
42 to 50	3 x Residual block		

Table 4-2.: Description of the ResNet50 architecture.

4.2.3. Classification of endoscopic ultrasound images by transfer learning

This process is described in subsection 4.1.1, but in this case, the number of neurons in the final layer is three, corresponding to classes in this problem: pancreatic cancer, pancreatitis, and normal tissue.

4.2.4. Results

The performance of the proposed methodology is evaluated by comparing the labels predicted by the method with the annotations made by the specialist. The methodology is assessed using the database described in section 2. In summary, the database includes 55 subjects. Among them, 32 patients are diagnosed with healthy pancreas or normal pancreas(NP), 18 patients with Pancreatic Cancer(PC), and 5 patients with pancreatitis(CP). In total, the database is composed of 66,249 frames, 16,585 with PC, 7,474 with CP, and 42,190 with NP.

Experimental Setup

The method was evaluated under a cross-validation scheme of 5 iterations. Each iteration distributes 75 % of the data for training and 25 % for testing. Additionally, 9 % of the training data was used to validate the networks at each epoch. The proportion of samples

from classes is balanced to avoid overfitting the network. To ensure this, pancreatitis case frames were duplicated using data augmentation, in which new frames are generated by applying a horizontal mirror transformation to the original data. Additionally, frames of normal tissue cases were randomly subsampled. Thus, a total of 45,557 frames were used to evaluate the proposed method, distributed as: 14,024 with normal tissue, 14,948 with pancreatitis (7,474 original images, plus the same value of transformed images), and 16,585 with pancreatic cancer.
The convolutional neural network was configured as follows:

- The selected architecture was ResNet50.
- The net was initialized with pre-trained weights with the ImageNet database [61].
- The loss function was cross-entropy.
- The optimization algorithm was stochastic gradient descent.
- The learning rate is reduced during the training stage using the exponential reduction strategy, configured with a reduction factor at every epoch.
- A weight decay strategy was applied.

Additionally, a grid search strategy was used to maximize the accuracy to achieve the optimal combination of 5 hyperparameters: a) initial learning rate, b) batch size), c) the decay factor of the weights, d) the factor, and e) the number of epochs of the learning rate reduction strategy [1]. This optimization process was carried out over 20 tests using 25 % of the training data for each iteration of the validation scheme. Subsequently, with the best hyperparameters found, complete training is performed for each iteration. Finally, the model with the highest validation accuracy over 40 epochs was chosen to be evaluated with the test data.

Quantitative evaluation

The convolutional neural network predicts a label for each frame: Normal tissue (class NP) represents frames of normal tissues from the pancreas, liver, and gallbladder, Pancreatitis (class CP), and pancreatic cancer (class PC). To quantify the performance of the network, the predicted label of each image is compared with the expert annotation, calculating average value per class and a global result of the accuracy, specificity, sensitivity, F-score and precision. The results are shown in Table **4-3**. The proposed method classifies the three classes outstandingly, obtaining an average accuracy of 84.8 %. Also, knowing that the main objective of this work is the detection of pancreatic cancer, the method obtained the highest F-score for this class, with 83.1 %. Additionally, the class with the lowest F-score was pancreatitis. This result could be explained by the low number of cases available to train the model. However, the proposed method was able to handle the high variability of the Normal

Tissue class and differentiate between the two abnormalities, pancreatitis and pancreatic cancer.

Class	Acc. (%)	Sens. (%)	Spec. (%)	Prec. (%)	F1 (%)
NP	$79,5 \pm 8,4$	$71,0 \pm 14,1$	$84,2 \pm 13,9$	$75,6 \pm 17,5$	$72,5 \pm 12,9$
CP	$90,1 \pm 10,1$	$76,5 \pm 30,5$	$95,2 \pm 2,7$	$65,3 \pm 21,2$	$65,5 \pm 21,9$
PC	$84,3 \pm 7,2$	$86,4 \pm 16,6$	$83,3 \pm 10,5$	$82,8 \pm 11,5$	$83,1 \pm 9,8$
Total	$84,8 \pm 7,8$	$78,9 \pm 14,1$	$87,6 \pm 5,8$	$74,7 \pm 11,4$	$73,7 \pm 13,0$

Table 4-3.: Proposed method results of each class and the total average.

4.2.5. Conclusions

The performance of state of the art methods depends on the way of the specialist search for anomalies in the EUS procedures and select specific frames with clear lesions. Nevertheless, the proposed method does not perform a preselection of images, providing the possibility of assisting a complete examination, alerting the expert if there is a malignant mass regardless if the lesion is partially occluded or blurred. However, the main limitation of this work is the amount of data used to evaluate the methodology[43, 82, 5, 39]. But none of the databases used by the state of the art methods are publicly accessible.

The proposed method applies deep learning techniques in videos of patients with pancreatic cancer confirmed by pathology, patients with normal pancreas, and patients with pancreatitis. In this task, the reached average accuracy was 84.3 % for pancreatic cancer, 90.1 % for pancreatitis, and 79.5 % for normal pancreas, obtaining an overall average accuracy of 84.8 %. The results obtained with the proposed method are highly competitive compared with state of the art methods. Also, the performance is superior in terms of the performed task complexity because the methodology is applied in complete Echoendoscopy video sequences, capturing the full variability of the endoscopic ultrasound procedures, which is close to a real scenario of EUS procedures. In future work, this technique could evolve into a real-time tool that improves exam performance.

5. Conclusions

This work presents a novel methodology to perform an exhaustive and fine-tuned multi-scale characterization of the echo patterns in EUS images, correlating them at different scales, positions, and orientations. The robust characterization feeds classical binary machine learning models that remarkably differentiate the tumoral echo patterns. The method was compared with deep learning-based frameworks of the state of the art, achieving competitive results and being less sensitive to typical noises of the ultrasound domain. Also, the proposed method is an automatic strategy, in contrast with the state of the art methods that require a pre-selection of frames. Therefore, the method is close to a real clinical scenario and could be adapted to support the diagnosis of pancreatic cancer in a gastroenterology unit.

In addition, in this work was constructed the first public database of Echoendoscopy images of the pancreas, including cases of patients with pancreatic cancer confirmed by histopathology analysis, patients with pancreatitis, and patients with a healthy pancreas.

Finally, future work and perspectives include the development of a strategy to localize the tumoral zone in detected frames using the multi-scale characterization of echo patterns. Also, feed the database with more cases, especially pancreatitis cases, adapting the method to solve the multi-class problem. In addition, the computational cost of the method may be optimized to be used as a real-time application, migrating to a compiled programming language.

A. Annexed: Detailed Patient Information

Label	Category	Frames	Age (years)	Gender	Endoscopic Diagnose	Symptoms							
						Abdominal pain	Jaundice	Emesis	Weight loss	Diarrhea	Other	None	Not Reported
C01	PC	399	50	F	Mass in the head of pancreas								X
C02	PC	269	87	M	Mass in the head of pancreas								X
C03	PC	1700	63	F	Mass in the head of pancreas								X
C04	PC	1319	68	M	Mass in the head of pancreas								X
C05	PC	539	50	M	Mass in the head of pancreas								X
C06	PC	570	75	M	Mass in the head of pancreas								X
C07	PC	1251	71	M	Mass in the head of pancreas								X
C08	PC	3619	63	F	Mass in the head of pancreas								X
C09	PC	247	75	F	Mass in the head of pancreas								X
C10	PC	607	60	M	Mass in the tail of pancreas	X			X				
C11	PC	2798	64	M	Tumor of the head of pancreas-hepatic metastasis	X		X					
C12	PC	395	60	F	Mass in head of pancreas, ascitis, hepatic cirrhosis	X					X		
C13	PC	739	69	F	Uncinated process lesion	X			X				
C14	PC	328	65	M	Body of pancreas lesion	X							
C15	PC	435	45	M	Body of pancreas lesion	X							

Label	Category	Frames	Age (years)	Gender	Endoscopic Diagnose	Symptoms							
						Abdominal pain	Jaundice	Emesis	Weight loss	Diarrhea	Other	None	Not Reported
C16	PC	157	80	M	Pancreatic head mass, pancreatic mass puncture and pancreatic liquid	X							
C17	PC	907	64	F	Pancreatic head mass, punction pancreatic mass and pancreatic fluid	X	X						
C18	PC	306	69	F	Distal coledocial lesion extending to the head of the pancreas, thickened coledoci	X		X					
H01	NP	588	44	F	Cholelithiasis without cholecystitis, negative exam for choledocolithiasis								X
H02	NP	2609	63	F	Mild ascitis							X	
H03	NP	28	59	F	Mucous fold in the background							X	
H04	NP	1046	57	F	Normal	X							
H05	NP	1000	74	F	Normal	X							
H06	NP	569	47	F	Normal							X	
H07	NP	81	40	M	Normal								X
H08	NP	900	27	F	Vesicular polyp	X							
H09	NP	660	28	M	Normal	X	X				X		
H10	NP	1504	84	M	Normal								X
H11	NP	617	61	M	Vesicular polyp	X							
H12	NP	1071	72	M	Gastric mucosa lesion in cardias, subepithelial lesion compatible with high grade gist							X	

Label	Category	Frames	Age (years)	Gender	Endoscopic Diagnose	Symptoms							
						Abdominal pain	Jaundice	Emesis	Weight loss	Diarrhea	Other	None	Not Reported
H13	NP	112	36	M	Normal		X						
H14	NP	3385	72	M	Normal	X							
H15	NP	2714	80	F	Normal	X	X				X		
H16	NP	732	60	F	Normal	X							
H17	NP	1624	53	F	Normal	X					X		
H18	NP	2396	66	F	Lipoma compatible with third layer subepithelial lesion								X
H19	NP	2175	82	F	Dilated choledochus, negative for choledocolithiasis or periampular lesions, hepatic lesions under study	X			X				
H20	NP	397	65	F	Normal	X	X	X					
H21	NP	1569	53	F	Early gastric lesion 0-IIC	X			X				
H22	NP	490	73	F	Normal	X				X			
H23	NP	820	51	F	Normal						X		
H24	NP	1700	41	F	Normal	X							
H25	NP	2765	48	M	Normal								X
H26	NP	327	26	M	Vesicular polyps							X	
H27	NP	1481	32	F	Vesicular polyps	X							
H28	NP	2805	28	F	Vesicular microlithiasis	X					X		
H29	NP	945	33	M	Normal	X							
H30	NP	1737	29	F	Normal			X		X	X		
H31	NP	404	33	F	Normal	X							
H32	NP	2939	28	M	Normal	X							

Label	Category	Frames	Age (years)	Gender	Endoscopic Diagnose	Symptoms							
						Abdominal pain	Jaundice	Emesis	Weight loss	Diarrhea	Other	None	Not Reported
P01	CP	740	48	F	Chronic pancreatitis and pancreatic lithiasis								X
P02	CP	3661	36	M	Chronic pancreatitis	X		X		X			
P03	CP	1751	60	M	Chronic pancreatitis	X							
P04	CP	412	49	M	Chronic pancreatitis	X		X					
P05	CP	910	36	M	Chronic pancreatitis and vesicular polyps								X

Table A-1.: Clinical patient information categorized in three grpoups Pancreatic Cancer (PC), Normal Pancreas (NP), and Chronic Pancreatitis (CP). See section 2

B. Annexed: Tumoral Information of patients with Pancreatic Cancer

Label	TNM Score	Tumor Size (mm)	Lesion Locate	Pathology
C01	T4NXM1	40x40	Head	Suspicious of adenocarcinoma
C02	T3NXM1	22x18	Head	Suspicious of adenocarcinoma
C03	T2N0M1	34x30	Head	Suspicious of adenocarcinoma
C04	T1N0MX	15x24	Head	Suspicious of adenocarcinoma
C05	T3N0MX	32x25	Head	The smears show a hemorrhagic background with frequent atypical ductal cells with hyperchromatic nuclei, discohesive, suggesting acini, others in bilayer, with lymphocytes, and few epithelial cells without atypia. DIAGNOSIS: head lesion to the pancreas. ACAF: Positive for malignancy "favors adenocarcinoma"
C06	T3N1MX	35x35	Head	The smears show a slightly hemorrhagic background with sheets of atypical epithelial cells with hyperchromatic nuclei, granular eosinophilic cytoplasm, loss of the nucleus-cytoplasm relationship, some forming acini, accompanied by another group of benign cells. Lymphocytes, histiocytes, and occasional neutrophil polymorphonuclear cells. DIAGNOSIS: head lesion to the pancreas. ACAF: Positive for malignancy "favors adenocarcinoma"

Label	TNM Score	Tumor Size (mm)	Lesion Locate	Pathology
C07	NR	40x40	Head	The smears are hypercellular with a hemorrhagic and proteinaceous background, made up of ductal epithelial cells, arranged in groups and sheets, with loss of the nucleus-cytoplasm relationship and nuclear hyperchromatism, others small with pyknotic nuclei, accompanied by inflammatory cells of the lymphohistiocytic and polymorphonuclear type. DIAGNOSIS: head lesion to the pancreas. BACAF: Positive for malignancy "favors adenocarcinoma"
C08	T3N0MX	26x24	Head	Extended hypercellular cells with a proteinaceous and slightly hemorrhagic background, made up of acinar and ductal epithelial cells, some of them with loss of the nucleus-cytoplasm relationship and nuclear hyperchromatism, arranged in sheets and groups of different sizes, accompanied by inflammatory cells of the lymphohistiocytic type. DIAGNOSIS: head lesion to the pancreas. BACAF: Positive for malignancy "favors adenocarcinoma"
C09	T3N0MX	25x25	Head	Extended hypercellular cells, with a hemorrhagic background, made up of ductal epithelial cells, arranged in groups, sheets, others loose, with loss of the nucleus-cytoplasm relationship, nuclear hyperchromatism, and overlap, mixed with polymorphonuclear cells, lymphocytes and foamy histiocytes. DIAGNOSIS: head lesion to the pancreas. ACAF: Positive for malignancy "favors adenocarcinoma"
C10	T4N1M1	40x40	Tail	Pancreas (cell block) - DIAGNOSIS: Carcinoma compromise
C11	T3NXM2	NR	Head	Aspiration cytology - DIAGNOSIS: Category IV: Suspect of mucinous neoplasm with focal atypia (Papanicolau Cytopathology Society Classification)

Label	TNM Score	Tumor Size (mm)	Lesion Locate	Pathology
C12	T3N0MX	44x38	Head	Pancreas (cell block) - Groups of epithelial cells with loss of honeycomb pattern, overlap, anisocytosis, nuclear hyperchromasia. There are no prominent nucleoli. There is a tendency to discohesiveness. Focally, cellular debris is identified in the background. Atypical epithelial cells suspected of adenocarcinoma. DIAGNOSIS: The described findings are interpreted as well differentiated adenocarcinoma.
C13	T1N1MX	20x20	Head	Malignant epithelial tumor constituted by small and medium-sized glands of irregular shape, which are composed of cells with pleomorphic and vesicular nuclei, with prominent nucleolus, which are arranged in a desmoplastic stroma with lymphocytes and neutrophilic PMNs; associated there is extension to the peripancreatic fat and the wall of the duodenum to the submucosa. DIAGNOSIS: Well differentiated infiltrating ductal adenocarcinoma.
C14	T3N0MX	37x37	Body	DIAGNOSIS: findings suspicious for malignancy
C15	T3N0M1	NR	Body	Pancreas - DIAGNOSIS: ACAF - Category V: Suspect for adenocarcinoma (Paris System)
C16	T3N1MX	NR	Head	There is little material consisting predominantly of fibrin and red blood cells with occasional polygonal cells with bulky hyperchromatic nuclei, some with prominent nucleoli and scant cytoplasm. DIAGNOSIS: These findings correlated with other studies result in pathology suspected of malignancy
C17	T3N1MX	NR	Head	Cytological study of a mass in the head of the pancreas - DIAGNOSIS: Category V: Suspect for ductal carcinoma
C18	NR	NR	Head	Pancreas - DIAGNOSIS: ACAF, Category V: Suspicious of malignancy, the findings described are suspicious of adenocarcinoma

Table B-1.: Tumoral information of Pancreatic cancer patients. Not reported size is labelled as NR. See section 2

C. Annexed: Noise Results

Model	Metric	Original	Speckle Noise				White Noise			
			1 %	10 %	20 %	30 %	1 %	10 %	20 %	30 %
Adaboost	Acc(%)	94,9	94,9	94,9	95,2	95,2	94,4	95,3	93,0	87,6
	Sens(%)	95,1	94,9	94,7	95,5	95,7	94,3	96,4	96,0	98,0
	Spec(%)	94,8	94,9	95,1	94,9	94,7	94,6	94,2	89,9	77,3
	F(%)	94,9	94,8	94,9	95,2	95,2	94,4	95,3	93,2	88,7
	Prec(%)	94,7	94,8	95,0	94,9	94,7	94,5	94,3	90,4	81,0
	NPV(%)	95,1	94,9	94,8	95,5	95,7	94,4	96,3	95,8	97,6
SVM with Linear kernel	Acc(%)	95,6	95,5	95,2	95,6	95,4	95,3	95,4	94,5	88,4
	Sens(%)	96,8	96,3	95,7	96,6	96,7	95,8	96,8	97,9	99,7
	Spec(%)	94,4	94,7	94,7	94,6	94,2	94,8	94,0	91,2	77,3
	F(%)	95,6	95,5	95,2	95,6	95,5	95,3	95,4	94,7	89,6
	Prec(%)	94,5	94,7	94,7	94,7	94,2	94,8	94,1	91,6	81,3
	NPV(%)	96,8	96,3	95,7	96,5	96,7	95,8	96,7	97,8	99,6
SVM with RBF kernel	Acc(%)	95,1	95,2	95,0	95,4	95,0	95,1	95,1	94,2	88,1
	Sens(%)	96,1	95,7	95,5	96,3	96,0	95,6	96,1	97,7	99,4
	Spec(%)	94,2	94,6	94,5	94,5	94,0	94,6	94,1	90,8	76,9
	F(%)	95,2	95,2	95,0	95,5	95,0	95,1	95,1	94,4	89,2
	Prec(%)	94,2	94,6	94,5	94,6	94,1	94,6	94,2	91,3	81,0
	NPV(%)	96,1	95,7	95,5	96,3	95,9	95,6	96,1	97,6	99,2

Table C-1.: Performance metrics of the proposed method when the testing set is contaminated with speckle and white noise. See section 3.2.2

Model	Metric	Original	Speckle Noise				White Noise			
			1 %	10 %	20 %	30 %	1 %	10 %	20 %	30 %
GoogleNet	Acc(%)	92.7	92.6	92.4	92.2	90.9	92,2	92,5	74,6	61,5
	Sens(%)	91.4	91.4	91.7	92.7	94.4	90,7	92,3	98,5	99,9
	Spec(%)	93.9	93.7	93.1	91.8	87.4	93,7	92,7	51,0	23,5
	F(%)	92.5	92.4	92.3	92.2	91.2	92,1	92,5	79,4	72,1
	Prec(%)	93.7	93.5	92.9	91.8	88.1	93,5	92,6	66,5	56,4
	NPV(%)	91.7	91.7	91.9	92.7	94.1	91,1	92,4	97,2	99,6
Resnet18	Acc(%)	77.9	78.0	77.4	77.3	78.6	73,4	74,0	59,3	53,0
	Sens(%)	59.3	59.6	58.2	58.2	61.4	47,8	51,2	22,0	6,5
	Spec(%)	96.2	96.2	96.3	96.2	95.5	98,8	96,5	96,2	98,9
	F(%)	72.7	72.9	71.9	71.8	74.0	64,2	66,2	34,9	12,2
	Prec(%)	94.0	94.0	94.0	93.8	93.2	97,4	93,5	85,2	85,4
	NPV(%)	70.5	70.6	70.0	69.9	71.4	65,7	66,7	55,5	51,7
Resnet50	Acc(%)	90,0	89.9	84.4	75.2	73.4	90,4	58,9	74,4	70,8
	Sens(%)	84.4	84.2	71.8	52.6	48.9	87,7	17,5	55,4	79,0
	Spec(%)	95.4	95.4	96.7	97.5	97.6	93,1	99,9	93,1	62,8
	F(%)	89.3	89.2	82.0	67.8	64.6	90,1	29,7	68,3	72,9
	Prec(%)	89.3	89.2	82.0	67.8	64.6	92,6	99,5	88,9	67,7
	NPV(%)	86.1	86.0	77.6	67.5	65.9	88,5	55,0	67,9	75,1

Table C-2.: Performance metrics of the baseline models when the testing set is contaminated with speckle and white noise. See section 3.2.2

Bibliography

[1] Akiba, Takuya ; Sano, Shotaro ; Yanase, Toshihiko ; Ohta, Takeru ; Koyama, Masanori: Optuna: A Next-generation Hyperparameter Optimization Framework, 2019. – ISBN 978–1–4503–6201–6, p. 2623–2631

[2] Amin, Sunil ; DiMaio, Christopher J. ; Kim, Michelle K.: Advanced EUS Imaging for Early Detection of Pancreatic Cancer. En: *Gastrointestinal Endoscopy Clinics of North America* 23 (2013), Nr. 3, p. 607 – 623. – ISSN 1052–5157

[3] Bafaraj, Ahmed S.: Performance Analysis of Best Speckle Filter for Noise Reduction in Ultrasound Medical Images. En: *International Journal of Applied Engineering Research* 14 (2019), p. 1340–1351. – ISSN 0973–4562

[4] Bay, Herbert ; Ess, Andreas ; Tuytelaars, Tinne ; Gool, Luc V.: Speeded-Up Robust Features (SURF). En: *Computer Vision and Image Understanding* 110 (2008), Nr. 3, p. 346 – 359. – Similarity Matching in Computer Vision and Multimedia. – ISSN 1077–3142

[5] Brand, B ; Pfaff, T ; Binmoeller, KF ; Sriram, PVJ ; Fritscher-Ravens, A ; Knöfel, WT ; Jäckle, S ; Soehendra, N: Endoscopic ultrasound for differential diagnosis of focal pancreatic lesions, confirmed by surgery. En: *Scandinavian journal of gastroenterology* 35 (2000), Nr. 11, p. 1221–1228

[6] Bray, Freddie ; Ferlay, Jacques ; Soerjomataram, Isabelle ; Siegel, Rebecca L. ; Torre, Lindsey A. ; Jemal, Ahmedin: Global cancer statistics 2018: GLOBOCAN estimates of incidence and mortality worldwide for 36 cancers in 185 countries. En: *CA: A Cancer Journal for Clinicians* 68 (2018), Nr. 6, p. 394–424

[7] Instituto Nacional de Cancerología, Instituto Geográfico Agustín C.: *Atlas de mortalidad por cáncer en Colombia*. Fourth. 2017

[8] Chen, Chien-Hua: EUS in Diagnosis and Treatment of GI Tract. En: *Ultrasound in Medicine & Biology* 43 (2017), p. S147. – ISSN 0301–5629

[9] Chen, Wei-Ming ; Chang, Ruey-Feng ; Kuo, Shou-Jen ; Chang, Cheng-Shyong ; Moon, Woo K. ; Chen, Shou-Tung ; Chen, Dar-Ren: 3-D ultrasound texture classification using run difference matrix. En: *Ultrasound in Medicine Biology* 31 (2005), Nr. 6, p. 763 – 770. – ISSN 0301–5629

[10] Chen, Xu ; Hu, Yiqun ; Zhang, Zhihong ; Wang, Beizhan ; Zhang, Lichi ; Shi, Fei ; Chen, Xinjian ; Jiang, Xiaoyi: A graph-based approach to automated EUS image layer segmentation and abnormal region detection. En: *Neurocomputing* 336 (2019), p. 79 – 91. – Advances in Graph Algorithm and Applications. – ISSN 0925–2312

[11] Costache, M-I ; Săftoiu, A ; Gheonea, D-I: Detection and Characterization of Solid Pancreatic Lesions (Contrast-Enhancement, Elastography, EUS-Guided Fine Needle Aspiration). En: *Video Journal and Encyclopedia of GI Endoscopy* 1 (2013), Nr. 2, p. 545–547. – Special Issue: Expert Encyclopedia â€“ Lower GI Tract, Bile Duct and Ampullary Region. – ISSN 2212–0971

[12] Cui, Xin-Wu ; Chang, Jian-Min ; Kan, Quan-Cheng ; Chiorean, Liliana ; Ignee, Andre ; Dietrich, Christoph F.: Endoscopic ultrasound elastography: Current status and future perspectives. En: *World journal of gastroenterology* 21 (2015), Nr. 47, p. 13212

[13] Dallongeville, Axel ; Corno, Lucie ; Silvera, Stéphane ; Boulay-Coletta, Isabelle ; Zins, Marc: Initial Diagnosis and Staging of Pancreatic Cancer Including Main Differentials. En: *Seminars in Ultrasound, CT and MRI* 40 (2019), Nr. 6, p. 436 – 468. – ISSN 0887–2171

[14] Das, Ananya ; Nguyen, Cuong C. ; Li, Feng ; Li, Baoxin: Digital image analysis of EUS images accurately differentiates pancreatic cancer from chronic pancreatitis and normal tissue. En: *Gastrointestinal Endoscopy* 67 (2008), Nr. 6, p. 861 – 867. – ISSN 0016–5107

[15] Deng, J. ; Dong, W. ; Socher, R. ; Li, L.-J. ; Li, K. ; Fei-Fei, L.: ImageNet: A Large-Scale Hierarchical Image Database. En: *CVPR09*, 2009

[16] DeWitt, John ; Devereaux, Benedict M. ; Lehman, Glen A. ; Sherman, Stuart ; Imperiale, Thomas F.: Comparison of Endoscopic Ultrasound and Computed Tomography for the Preoperative Evaluation of Pancreatic Cancer: A Systematic Review. En: *Clinical Gastroenterology and Hepatology* 4 (2006), p. 717 – 725

[17] Giovannini, M. ; Hookey, L. ; Bories, E. ; Pesenti, C. ; Monges, G. ; Delpero, J.: Endoscopic Ultrasound Elastography: the First Step towards Virtual Biopsy? Preliminary Results in 49 Patients. En: *Endoscopy* 38 (2006), Nr. 4, p. 344–348

[18] Giovannini, Marc ; Botelberge, Thomas ; Bories, Erwan ; Pesenti, Christian ; Caillol, Fabrice ; Esterni, Benjamin ; Monges, Geneviève ; Arcidiacono, Paolo ; Deprez, Pierre ; Yeung, Robert ; Schimdt, Walter ; Schrader, Hanz ; Szymanski, Carl ; Dietrich, Christoph ; Eisendrath, Pierre ; Laethem, Jean-Luc V. ; Devière, Jacques ; Vilmann, Peter ; Saftoiu, Adrian: Endoscopic ultrasound elastography for

evaluation of lymph nodes and pancreatic masses: A multicenter study. En: *World Journal of Gastroenterology* 15 (2009), Nr. 13, p. 1587

[19] Goggins, Michael ; Overbeek, Kasper A. ; Brand, Randall ; Syngal, Sapna ; Chiaro, Marco D. ; Bartsch, Detlef K. ; Bassi, Claudio ; Carrato, Alfredo ; Farrell, James ; Fishman, Elliot K. ; Fockens, Paul ; Gress, Thomas M. ; van Hooft, Jeanin E. ; Hruban, R H. ; Kastrinos, Fay ; Klein, Allison ; Lennon, Anne M. ; Lucas, Aimee ; Park, Walter ; Rustgi, Anil ; Simeone, Diane ; Stoffel, Elena ; Vasen, Hans F A. ; Cahen, Djuna L. ; Canto, Marcia I. ; Bruno, Marco: Management of patients with increased risk for familial pancreatic cancer: updated recommendations from the International Cancer of the Pancreas Screening (CAPS) Consortium. En: *Gut* 69 (2019), Oktober, Nr. 1, p. 7–17

[20] Guo, J. ; Sun, Siyu: Endoscopic Ultrasound for the Diagnosis of Chronic Pancreatitis, Pancreapedia: Exocrine Pancreas Knowledge Base, 2015

[21] Han, Seokmin ; Kang, Ho-Kyung ; Jeong, Ja-Yeon ; Park, Moon-Ho ; Kim, Wonsik ; Bang, Won-Chul ; Seong, Yeong-Kyeong: A deep learning framework for supporting the classification of breast lesions in ultrasound images. En: *Physics in Medicine &amp Biology* 62 (2017), sep, Nr. 19, p. 7714–7728

[22] Harinck, F ; Konings, I C A W. ; Kluijt, I ; Poley, J W. ; van Hooft, J E. ; van Dullemen, H M. ; Nio, C Y. ; Krak, N C. ; Hermans, J J. ; Aalfs, C M. ; Wagner, A ; Sijmons, R H. ; Biermann, K ; van Eijck, C H. ; Gouma, D J. ; Dijkgraaf, M G W. ; Fockens, P ; Bruno, M J.: A multicentre comparative prospective blinded analysis of EUS and MRI for screening of pancreatic cancer in high-risk individuals. En: *Gut* 65 (2015), Mai, Nr. 9, p. 1505–1513

[23] He, Kaiming ; Zhang, Xiangyu ; Ren, Shaoqing ; Sun, Jian: Deep Residual Learning for Image Recognition. En: *2016 IEEE Conference on Computer Vision and Pattern Recognition (CVPR)*, 2016, p. 770–778

[24] In: Hermanek, P. ; Hutter, R. V. P. ; Sobin, L. H. ; Wagner, G. ; Wittekind, Ch.: *Digestive System Tumours*. Berlin, Heidelberg : Springer Berlin Heidelberg, 1997, p. 71–152. – ISBN 978–3–662–03432–3

[25] Hidalgo, Manuel: Pancreatic Cancer. En: *New England Journal of Medicine* 362 (2010), Nr. 17, p. 1605–1617

[26] Hirche, T. ; Ignee, A. ; Barreiros, A. ; Schreiber-Dietrich, D. ; Jungblut, S. ; Ott, M. ; Hirche, H. ; Dietrich, C.: Indications and limitations of endoscopic ultrasound elastography for evaluation of focal pancreatic lesions. En: *Endoscopy* 40 (2008), November, Nr. 11, p. 910–917

[27] Iglesias-Garcia, Julio ; Larino-Noia, Jose ; Abdulkader, Ihab ; Forteza, Jeronimo ; Dominguez-Munoz, J. E.: EUS elastography for the characterization of solid pancreatic masses. En: *Gastrointestinal Endoscopy* 70 (2009), Dezember, Nr. 6, p. 1101–1108

[28] Iglesias-García, Julio ; no Noia, Jose L. ; noz, Juan Enrique Domínguez-Mu New Imaging Techniques: Endoscopic Ultrasound-Guided Elastography. En: *Gastrointestinal Endoscopy Clinics of North America* 27 (2017), p. 551 – 567

[29] Iglesias–Garcia, Julio ; Larino–Noia, Jose ; Abdulkader, Ihab ; Forteza, Jeronimo ; Dominguez–Munoz, J. E.: Quantitative Endoscopic Ultrasound Elastography: An Accurate Method for the Differentiation of Solid Pancreatic Masses. En: *Gastroenterology* 139 (2010), Oktober, Nr. 4, p. 1172–1180

[30] Ihnatsenka, Barys ; Boezaart, Andre: Ultrasound: Basic understanding and learning the language. En: *International journal of shoulder surgery* 4 (2010), 07, p. 55–62

[31] Jain, Akriti G. ; Saleem, Tabinda ; Kumar, Ranjeet ; Khetpal, Neelam ; Zafar, Hammad ; Rashid, Mamoon U. ; Ali, Saeed ; Majeed, Umair ; Ahmad, Sarfraz: En: *Breaking Tolerance to Pancreatic Cancer Unresponsiveness to Chemotherapy* Vol. 5. 2019, p. 1 – 11

[32] Janssen, Jan ; Schlörer, Eva ; Greiner, Lucas: EUS elastography of the pancreas: feasibility and pattern description of the normal pancreas, chronic pancreatitis, and focal pancreatic lesions. En: *Gastrointestinal Endoscopy* 65 (2007), Juni, Nr. 7, p. 971–978

[33] Jaramillo, María ; Ruano, Josué ; Gómez, Martín ; Romero, Eduardo: Endoscopic ultrasound database of the pancreas. En: *16th International Symposium on Medical Information Processing and Analysis* Vol. 11583 International Society for Optics and Photonics, 2020, p. 115830G

[34] Jaramillo, María ; Ruano, Josué ; M.D., Martín G. ; Romero, Eduardo: Automatic detection of pancreatic tumors in endoscopic ultrasound videos using deep learning techniques. En: Bottenus, Nick (Ed.) ; Ruiter, Nicole V. (Ed.): *Medical Imaging 2022: Ultrasonic Imaging and Tomography* Vol. 12038 International Society for Optics and Photonics, SPIE, 2022, p. 106 – 115

[35] Kawada, Natsuko ; Tanaka, Sachiko: Elastography for the pancreas: Current status and future perspective. En: *World J Gastroenterol* 22 (2016), p. 3712â€“3724

[36] Kitano, Masayuki ; Yamashita, Yasunobu: New Imaging Techniques for Endoscopic Ultrasonography: Contrast-Enhanced Endoscopic Ultrasonography. En: *Gastrointesti-*

nal Endoscopy Clinics of North America 27 (2017), Nr. 4, p. 569–583. – Progress in Endoscopic Ultrasonography. – ISSN 1052–5157

[37] Kitano, Masayuki ; Yoshida, Takeichi ; Itonaga, Masahiro ; Tamura, Takashi ; Hatamaru, Keiichi ; Yamashita, Yasunobu: Impact of endoscopic ultrasonography on diagnosis of pancreatic cancer. En: *Journal of gastroenterology* 54 (2019), Nr. 1, p. 19–32

[38] Kuwahara, Takamichi ; Hara, Kazuo ; Mizuno, Nobumasa ; Haba, Shin ; Okuno, Nozomi ; Koda, Hiroki ; Miyano, Akira ; Fumihara, Daiki: Current status of artificial intelligence analysis for endoscopic ultrasonography. En: *Digestive Endoscopy* (2020)

[39] Kuwahara, Takamichi ; Hara, Kazuo ; Mizuno, Nobumasa ; Okuno, Nozomi ; Matsumoto, Shimpei ; Obata, Masahiro ; Kurita, Yusuke ; Koda, Hiroki ; Toriyama, Kazuhiro ; Onishi, Sachiyo [u. a.]: Usefulness of Deep Learning Analysis for the Diagnosis of Malignancy in Intraductal Papillary Mucinous Neoplasms of the Pancreas. En: *Clinical and translational gastroenterology* 10 (2019), Nr. 5

[40] Lee, Jeffrey H. ; Ahmed, Osman: Endoscopic Management of Pancreatic Cancer. En: *Surgical Oncology Clinics of North America* 28 (2019), p. 147 – 159

[41] Lee, Linda S. ; Andersen, Dana K. ; Ashida, Reiko ; Brugge, William R. ; Canto, Mimi I. ; Chang, Kenneth J. ; Chari, Suresh T. ; DeWitt, John ; Hwang, Joo H. ; Khashab, Mouen A. [u. a.]: EUS and related technologies for the diagnosis and treatment of pancreatic disease: research gaps and opportunities-Summary of a National Institute of Diabetes and Digestive and Kidney Diseases workshop. En: *Gastrointestinal endoscopy* 86 (2017), Nr. 5, p. 768–778

[42] Liu, Mengchen ; Liu, Shixia ; Su, Hang ; Cao, Kelei ; Zhu, Jun. *Analyzing the Noise Robustness of Deep Neural Networks*. 2018

[43] Liu, Shengfeng ; Wang, Yi ; Yang, Xin ; Lei, Baiying ; Liu, Li ; Li, Shawn X. ; Ni, Dong ; Wang, Tianfu: Deep Learning in Medical Ultrasound Analysis: A Review. En: *Engineering* 5 (2019), Nr. 2, p. 261 – 275. – ISSN 2095–8099

[44] Llop, Esther ; Guerrero, Pedro ; Duran, AdriÃ ; Barrabes, Sílvia ; Massaguer, Anna ; Iglesias, María ; Quer, M.T. ; De Llorens, Rafael ; Peracaula, Rosa: Glycoprotein biomarkers for the detection of pancreatic ductal adenocarcinoma. En: *World Journal of Gastroenterology* 24 (2018), 06

[45] Mahadevan, Vishy: Anatomy of the pancreas and spleen. En: *Surgery (Oxford)* 37 (2019), Nr. 6, p. 297–301. – ISSN 0263–9319

[46] Maisonneuve, Patrick: Epidemiology and burden of pancreatic cancer. En: *La Presse Médicale* 48 (2019), p. e113 – e123

[47] Mateo, Juan L. ; Fernández-Caballero, Antonio: Finding out general tendencies in speckle noise reduction in ultrasound images. En: *Expert Systems with Applications* 36 (2009), Nr. 4, p. 7786 – 7797. – ISSN 0957–4174

[48] McGuckin, Ellen ; Cade, Jennifer E. ; Hanison, James: The pancreas. En: *Anaesthesia Intensive Care Medicine* 21 (2020), Nr. 11, p. 604–610. – ISSN 1472–0299

[49] Mei, Mei ; Ni, Jingmei ; Liu, Dan ; Jin, Piaopiao ; Sun, Leimin: EUS elastography for diagnosis of solid pancreatic masses: a meta-analysis. En: *Gastrointestinal endoscopy* 77 (2013), Nr. 4, p. 578–589

[50] Miura, Fumihiko ; Takada, Tadahiro ; Amano, Hodaka ; Yoshida, Masahiro ; Furui, Shigeru ; Takeshita, Koji: Diagnosis of pancreatic cancer. En: *HPB* 8 (2006), p. 337 – 342

[51] Moutinho-Ribeiro, Pedro ; Iglesias-Garcia, Julio ; Gaspar, Rui ; Macedo, Guilherme: Early pancreatic cancer - The role of endoscopic ultrasound with or without tissue acquisition in diagnosis and staging. En: *Digestive and Liver Disease* 51 (2019), p. 4 – 9

[52] Moutinho-Ribeiro, Pedro ; Liberal, Rodrigo ; Macedo, Guilherme: Endoscopic ultrasound in pancreatic cancer treatment: Facts and hopes. En: *Clinics and Research in Hepatology and Gastroenterology* 43 (2019), Nr. 5, p. 513 – 521. – ISSN 2210–7401

[53] Norton, Ian D. ; Zheng, Yi ; Wiersema, Maurits S. ; Greenleaf, James ; Clain, Jonathan E. ; DiMagno, Eugene P.: Neural network analysis of EUS images to differentiate between pancreatic malignancy and pancreatitis. En: *Gastrointestinal Endoscopy* 54 (2001), Nr. 5, p. 625 – 629. – ISSN 0016–5107

[54] Omary, M. B. ; Lugea, Aurelia ; Lowe, Anson W. ; Pandol, Stephen J.: The pancreatic stellate cell: a star on the rise in pancreatic diseases. En: *The Journal of Clinical Investigation* 117 (2007), 1, Nr. 1, p. 50–59

[55] Owens, David J. ; Savides, Thomas J.: Endoscopic Ultrasound Staging and Novel Therapeutics for Pancreatic Cancer. En: *Surgical Oncology Clinics of North America* 19 (2010), Nr. 2, p. 255 – 266. – ISSN 1055–3207

[56] Park, RichardD. ; Nyland, ThomasG. ; Lattimer, JimmyC. ; Miller, CharlesW. ; Lebel, JackL.: B-MODE GRAY-SCALE ULTRASOUND: IMAGING ARTIFACTS AND INTERPRETATION PRINCIPLES. En: *Veterinary Radiology* 22 (1981), Nr. 5, p. 204–210

[57] Patey, Susannah J. ; Corcoran, James P.: Physics of ultrasound. En: *Anaesthesia Intensive Care Medicine* 22 (2021), Nr. 1, p. 58–63. – ISSN 1472–0299

[58] Peng, Hanchuan ; Long, Fuhui ; Ding, Chris: Feature selection based on mutual information criteria of max-dependency, max-relevance, and min-redundancy. En: *IEEE Transactions on pattern analysis and machine intelligence* 27 (2005), Nr. 8, p. 1226–1238

[59] Rosenthal, Michael H. ; Lee, Alexander ; Jajoo, Kunal: Imaging and Endoscopic Approaches to Pancreatic Cancer. En: *Hematology/Oncology Clinics of North America* 29 (2015), Nr. 4, p. 675 – 699. – ISSN 0889–8588

[60] Ruano, Josué ; Jaramillo, María ; Gómez, Martín ; Romero, Eduardo: Robust Descriptor of Pancreatic Tissue for Automatic Detection of Pancreatic Cancer in Endoscopic Ultrasonography. En: *Ultrasound in Medicine Biology* (2022). – ISSN 0301–5629

[61] Russakovsky, Olga ; Deng, Jia ; Su, Hao ; Krause, Jonathan ; Satheesh, Sanjeev ; Ma, Sean ; Huang, Zhiheng ; Karpathy, Andrej ; Khosla, Aditya ; Bernstein, Michael ; Berg, Alexander C. ; Fei-Fei, Li: ImageNet Large Scale Visual Recognition Challenge. En: *International Journal of Computer Vision (IJCV)* 115 (2015), Nr. 3, p. 211–252

[62] Săftoiu, A. ; Vilmann, P. ; Gorunescu, F. ; Janssen, J. ; Hocke, M. ; Larsen, M. ; Iglesias-Garcia, J. ; Arcidiacono, P. ; Will, U. ; Giovannini, M. ; Dietrich, C. ; Havre, R. ; Gheorghe, C. ; McKay, C. ; Gheonea, D. ; Ciurea, T.: Accuracy of endoscopic ultrasound elastography used for differential diagnosis of focal pancreatic masses: a multicenter study. En: *Endoscopy* 43 (2011), März, Nr. 07, p. 596–603

[63] Săftoiu, Adrian ; Vilmann, Peter ; Dietrich, Christoph F. ; Iglesias-Garcia, Julio ; Hocke, Michael ; Seicean, Andrada ; Ignee, Andre ; Hassan, Hazem ; Streba, Costin T. ; Ioncică, Ana M. ; Gheonea, Dan I. ; Ciurea, Tudorel: Quantitative contrast-enhanced harmonic EUS in differential diagnosis of focal pancreatic masses (with videos). En: *Gastrointestinal Endoscopy* 82 (2015), Nr. 1, p. 59 – 69. – ISSN 0016–5107

[64] Săftoiu, Adrian ; Vilmann, Peter ; Gorunescu, Florin ; Gheonea, Dan I. ; Gorunescu, Marina ; Ciurea, Tudorel ; Popescu, Gabriel L. ; Iordache, Alexandru ; Hassan, Hazem ; Iordache, SevastiÅ£a: Neural network analysis of dynamic sequences of EUS elastography used for the differential diagnosis of chronic pancreatitis and pancreatic cancer. En: *Gastrointestinal Endoscopy* 68 (2008), Nr. 6, p. 1086 – 1094. – ISSN 0016–5107

[65] Săftoiu, Adrian ; Vilmann, Peter ; Gorunescu, Florin ; Janssen, Jan ; Hocke, Michael ; Larsen, Michael ; Iglesias–Garcia, Julio ; Arcidiacono, Paolo ; Will, Uwe ; Giovannini, Marc ; Dietrich, Cristoph F. ; Havre, Roald ; Gheorghe, Cristian ; McKay, Colin ; Gheonea, Dan I. ; Ciurea, Tudorel: Efficacy of an Artificial Neural Network–Based Approach to Endoscopic Ultrasound Elastography in Diagnosis of Focal Pancreatic Masses. En: *Clinical Gastroenterology and Hepatology* 10 (2012), Januar, Nr. 1, p. 84–90.e1

[66] Săftoiu, Adrian ; Vilmann, Peter ; Gorunescu, Florin ; Janssen, Jan ; Hocke, Michael ; Larsen, Michael ; IglesiasÂ€“Garcia, Julio ; Arcidiacono, Paolo ; Will, Uwe ; Giovannini, Marc ; Dietrich, Cristoph F. ; Havre, Roald ; Gheorghe, Cristian ; McKay, Colin ; Gheonea, Dan I. ; Ciurea, Tudorel: Efficacy of an Artificial Neural Networkâ€“Based Approach to Endoscopic Ultrasound Elastography in Diagnosis of Focal Pancreatic Masses. En: *Clinical Gastroenterology and Hepatology* 10 (2012), Nr. 1, p. 84 – 90.e1. – ISSN 1542–3565

[67] Sakamoto, Hiroki ; Kitano, Masayuki ; Suetomi, Yoichiro ; Maekawa, Kiyoshi ; Takeyama, Yoshifumi ; Kudo, Masatoshi: Utility of Contrast-Enhanced Endoscopic Ultrasonography for Diagnosis of Small Pancreatic Carcinomas. En: *Ultrasound in Medicine & Biology* 34 (2008), April, Nr. 4, p. 525–532

[68] Singh, Ajaypal ; Faulx, Ashley L.: Endoscopic Evaluation in the Workup of Pancreatic Cancer. En: *Surgical Clinics of North America* 96 (2016), Nr. 6, p. 1257 – 1270. – ISSN 0039–6109

[69] Singh, Karamjeet ; Ranade, Sukhjeet K. ; Singh, Chandan: A hybrid algorithm for speckle noise reduction of ultrasound images. En: *Computer Methods and Programs in Biomedicine* 148 (2017), p. 55–69. – ISSN 0169–2607

[70] Slack, J.M.: Developmental biology of the pancreas. En: *Development* 121 (1995), 06, Nr. 6, p. 1569–1580. – ISSN 0950–1991

[71] Stevens, Tyler ; Parsi, Mansour A.: Endoscopic ultrasound for the diagnosis of chronic pancreatitis. En: *World journal of gastroenterology* 16 (2010), Jun, Nr. 23, p. 2841–2850. – 20556829[pmid]. – ISSN 2219–2840

[72] Stevens, Tyler ; Parsi, Mansour A.: Endoscopic ultrasound for the diagnosis of chronic pancreatitis. En: *World journal of gastroenterology* 16 (2010), 06, p. 2841–50

[73] Stolzenberg-Solomon, Rachael Z. ; Amundadottir, Laufey T.: Epidemiology and Inherited Predisposition for Sporadic Pancreatic Adenocarcinoma. En: *Hematology/Oncology Clinics of North America* 29 (2015), Nr. 4, p. 619 – 640

[74] Sung, Hyuna ; Ferlay, Jacques ; Siegel, Rebecca L. ; Laversanne, Mathieu ; Soerjomataram, Isabelle ; Jemal, Ahmedin ; Bray, Freddie: Global Cancer Statistics 2020: GLOBOCAN Estimates of Incidence and Mortality Worldwide for 36 Cancers in 185 Countries. En: *CA: A Cancer Journal for Clinicians* 71 (2021), Nr. 3, p. 209–249

[75] Szegedy, Christian ; Liu, Wei ; Jia, Yangqing ; Sermanet, Pierre ; Reed, Scott ; Anguelov, Dragomir ; Erhan, Dumitru ; Vanhoucke, Vincent ; Rabinovich, Andrew: Going Deeper with Convolutions. En: *Computer Vision and Pattern Recognition (CVPR)*, 2015

[76] Takhar, Arjun S. ; Palaniappan, Ponni ; Dhingsa, Rajpal ; Lobo, Dileep N.: Recent developments in diagnosis of pancreatic cancer. En: *BMJ* 329 (2004), Nr. 7467, p. 668–673. – ISSN 0959–8138

[77] Tonozuka, Ryosuke ; Itoi, Takao ; Nagata, Naoyoshi ; Kojima, Hiroyuki ; Sofuni, Atsushi ; Tsuchiya, Takayoshi ; Ishii, Kentaro ; Tanaka, Reina ; Nagakawa, Yuichi ; Mukai, Shuntaro: Deep learning analysis for the detection of pancreatic cancer on endosonographic images: a pilot study. En: *Journal of Hepato-Biliary-Pancreatic Sciences* (2020)

[78] Walling, Anne ; Freelove, Robert: Pancreatitis and Pancreatic Cancer. En: *Primary Care: Clinics in Office Practice* 44 (2017), Nr. 4, p. 609 – 620. – ISSN 0095–4543

[79] Wani, Sachin ; Hall, Matthew ; Keswani, Rajesh N. ; Aslanian, Harry R. ; Casey, Brenna ; Burbridge, Rebecca ; Chak, Amitabh ; Chen, Ann M. ; Cote, Gregory ; Edmundowicz, Steven A. ; Faulx, Ashley L. ; Hollander, Thomas G. ; Lee, Linda S. ; Mullady, Daniel ; Murad, Faris ; Muthusamy, V. R. ; Pfau, Patrick R. ; Scheiman, James M. ; Tokar, Jeffrey ; Wagh, Mihir S. ; Watson, Rabindra ; Early, Dayna: Variation in Aptitude of Trainees in Endoscopic Ultrasonography, Based on Cumulative Sum Analysis. En: *Clinical Gastroenterology and Hepatology* 13 (2015), Nr. 7, p. 1318 – 1325.e2. – ISSN 1542–3565

[80] Wani, Sachin ; Han, Samuel ; Simon, Violette ; et al.: Setting minimum standards for training in EUS and ERCP: resultsÂ from a prospective multicenter study evaluating learningÂ curves and competence among advanced endoscopyÂ trainees. En: *Gastrointestinal Endoscopy* 89 (2019), Nr. 6, p. 1160 – 1168.e9. – ISSN 0016–5107

[81] Wani, Sachin ; Muthusamy, V. R. ; Komanduri, Srinadh: EUS-guided tissue acquisition: an evidence-based approach (with videos). En: *Gastrointestinal Endoscopy* 80 (2014), p. 939 – 959.e7

[82] Wen-Li Lee ; Yung-Chang Chen ; Kai-Sheng Hsieh: Ultrasonic liver tissues classification by fractal feature vector based on M-band wavelet transform. En: *IEEE*

Transactions on Medical Imaging 22 (2003), March, Nr. 3, p. 382–392. – ISSN 1558–254X

[83] Yasuda, Kenjiro ; Mukai, Hidekazu ; Nakajima, Masatsugu: Endoscopic Ultrasonography Diagnosis of Pancreatic Cancer. En: *Gastrointestinal Endoscopy Clinics of North America* 5 (1995), Nr. 4, p. 699 – 712. – ISSN 1052–5157

[84] Younan, George: Pancreas Solid Tumors. En: *Surgical Clinics of North America* 100 (2020), Nr. 3, p. 565–580. – Surgical Oncology for the General Surgeon. – ISSN 0039–6109

[85] Zhang, Jun ; Zhu, Liangru ; Yao, Liwen ; Ding, Xiangwu ; Chen, Di ; Wu, Huiling ; Lu, Zihua ; Zhou, Wei ; Zhang, Lihui ; An, Ping ; Xu, Bo ; Tan, Wei ; Hu, Shan ; Cheng, Fan ; Yu, Honggang: Deep-learningâ€“based pancreas segmentation and station recognition system in EUS: development and validation of a useful training tool (with video). En: *Gastrointestinal Endoscopy* (2020). – ISSN 0016–5107

[86] Zhang, Min-Min ; Yang, Hua ; Jin, Zhen-Dong ; Yu, Jian-Guo ; Cai, Zhe-Yuan ; Li, Zhao-Shen: Differential diagnosis of pancreatic cancer from normal tissue with digital imaging processing and pattern recognition based on a support vector machine of EUS images. En: *Gastrointestinal Endoscopy* 72 (2010), Nr. 5, p. 978 – 985. – ISSN 0016–5107

[87] Zhu, Maoling ; Xu, Can ; Yu, Jianguo ; Wu, Yijun ; Li, Chunguang ; Zhang, Minmin ; Jin, Zhendong ; Li, Zhaoshen: Differentiation of Pancreatic Cancer and Chronic Pancreatitis Using Computer-Aided Diagnosis of Endoscopic Ultrasound (EUS) Images: A Diagnostic Test. En: *PLOS ONE* 8 (2013), 05, Nr. 5, p. 1–6